

Prospects for detecting transient quasi-monochromatic gravitational waves from glitching pulsars with current and future detectors

Joan Moragues *, Luana M. Modafferi †, Rodrigo Tenorio ‡, David Keitel §

Departament de Física, Universitat de les Illes Balears, IAC3–IEEC, Crta. Valldemossa km 7.5, E-07122 Palma, Spain

dated 2022-12-16 – LIGO-P2200273-v5 – ET-0198D-22

This is a pre-copyedited, author-produced PDF of an article accepted for publication in MNRAS following peer review. The version of record (Monthly Notices of the Royal Astronomical Society, 2022; stac3665) is available online at: <https://doi.org/10.1093/mnras/stac3665>

ABSTRACT

Pulsars are rotating neutron stars that emit periodic electromagnetic radiation. While pulsars generally slow down as they lose energy, some also experience glitches: spontaneous increases of their rotational frequency. According to several models, these glitches can also lead to the emission of long-duration transient gravitational waves (GWs). We present detection prospects for such signals by comparing indirect energy upper limits on GW strain for known glitches with the sensitivity of current and future ground-based GW detectors. We first consider the optimistic case of generic constraints based on the glitch size and find that realistic matched-filter searches in the fourth LIGO–Virgo–KAGRA observing run (O4) could make a detection, or set constraints below these indirect upper limits, for equivalents of 36 out of 726 previously observed glitches, and 74 in the O5 run. With the third-generation Einstein Telescope or Cosmic Explorer, 35–40% of glitches would be accessible. When specialising to a scenario where transient mountains produce the post-glitch GW emission, following the Yim & Jones model, the indirect upper limits are stricter. Out of the smaller set of 119 glitches with measured healing parameter, as needed for predictions under that model, only 6 glitches would have been within reach for O4 and 14 for O5, with a similar percentage as before with third generation detectors. We also discuss how this model matches the observed glitch population.

Key words: gravitational waves – stars: neutron – pulsars: general – methods: data analysis

1 INTRODUCTION

Pulsars are highly magnetized neutron stars (NSs) that emit regular pulses of electromagnetic radiation as they spin (Lorimer & Kramer 2012). In general, their rotation slows down over time due to the energy loss from radiation, but sometimes they experience a sudden increase in rotational frequency: this phenomenon is known as a *glitch* (Link et al. 1992, 2000; Lyne et al. 2000; Fuentes et al. 2017). During a glitch, a pulsar can suffer not only an increase in its rotational frequency, but also a change in its spindown parameters (frequency derivatives). Glitches can be an ideal probe to understand the physics of NS interiors (Haskell 2017).

NSs in general are promising sources of gravitational wave (GW) emission (Glampedakis & Gualtieri 2018). One kind of GWs emitted from NSs are continuous waves (CWs). These are much fainter than the signals generated by compact binary coalescences (Abbott et al. 2021a), which is the main reason why they remain undetected up to date (Riles 2022). Improvements of the current LVK detectors – LIGO Livingston, LIGO Hanford, Virgo and KAGRA (Aasi et al. 2015; Acernese et al. 2015; Akutsu et al. 2019) – as well as the new detectors planned for the next decade (Abbott et al. 2017a; Adhikari et al. 2019) – like the Einstein Telescope (ET, Punturo et al. 2010) and Cosmic Explorer (CE, Reitze et al. 2019) – give more optimistic

predictions for the future (Pitkin 2011; Maggiore et al. 2020; Evans et al. 2021).

In this work we focus on long-duration transient CW-like signals (tCWs) from glitching pulsars. We do not cover short burst-like signals from f -modes, for which see Andersson & Kokkotas (1998); Ho et al. (2020a); Yim & Jones (2023); Lopez et al. (2022). Rather, we are interested in tCW signals that are quasi-monochromatic, like CWs, but with durations of hours to months (Prix et al. 2011). Such long-duration transient signals triggered by pulsar glitches are predicted by several models (van Eysden & Melatos 2008; Bennett et al. 2010; Melatos et al. 2015; Singh 2017; Yim & Jones 2020). The aim of this work is to estimate the detection prospects for such signals taking into account sensitivity upgrades to the current detector network and future detectors. This is complementary to a similar study done for CWs from known pulsars by Pitkin (2011). To do so, we build on past analyses of the population of known glitching pulsars (Fuentes et al. 2017; Ashton et al. 2017) using the most recent datasets of the ATNF and Jodrell Bank glitch catalogues (ATNF 2022; Shaw et al. 2022; Espinoza et al. 2011; Basu et al. 2022). We use this previously observed glitch population as a proxy for expected future glitches.

Our main detectability results are based on estimating the energy budget available from a glitch, for example within the two-fluid model for pulsar glitches, explained in Section 3. If we assume all this energy goes into the emitted GWs, we get a generic (and optimistic) upper limit for the amplitude of the signal. For all known glitches, we compare these indirect upper limits to the expected sensitivity of current and future detectors. To realistically determine the expected

* E-mail: joan.moragues@ligo.org

† E-mail: luana.modafferi@ligo.org

‡ E-mail: rodrigo.tenorio@ligo.org

§ E-mail: david.keitel@ligo.org

sensitivity of each detector to this particular type of signals, we consider a specific search method, the matched-filter transient \mathcal{F} -statistic (Prix et al. 2011), with realistic setups as previously used in real searches (Keitel et al. 2019; Abbott et al. 2022b; Modafferi et al. 2021). For different search methods the sensitivity will vary, but this is the method that has already been used in practice, and it also serves as a limiting case for the sensitivity achievable by other, more generic methods.

The paper is structured as follows: In Section 2, we present a brief overview of the known glitch population. In Section 3 we briefly review the physics behind pulsar glitches and their GW emission. Then, in Section 4 we go through some of the search methods for long-duration transient GWs. We then estimate detection prospects first based on generic indirect energy upper limits (Section 5) and then more specifically for the Yim & Jones (2020) transient mountain model (Section 6). In the latter, we also study how well that model matches the observed glitch population. We conclude in Section 7.

2 OBSERVED POPULATION OF GLITCHING PULSARS

Ideally, a study of future detection prospects would be based on a detailed modelling of the observed population of glitching pulsars or population synthesis simulations. We choose a simpler approach, using the previously observed set of glitches from the known pulsar population, assuming that future glitches will have similar characteristics to previous ones, and leaving a proper treatment of selection effects to future work. With the expected larger number of pulsars to be detected by new telescopes, like CHIME, SKA and FAST (Amiri et al. 2021; Keane et al. 2015; Zhu 2018), our estimates are likely to be pessimistic in terms of the total number of detectable signals. Conclusions drawn from this study should therefore be a conservative estimation of the expected number of detectable tCWs emitted by future glitches. For most glitches, we take information from the ATNF and Jodrell Bank glitch catalogues (ATNF 2022; Shaw et al. 2022; Espinoza et al. 2011; Basu et al. 2022). Both contain lists of glitches observed by various telescopes, but do not overlap exactly. In the versions downloaded for this work, the ATNF glitch catalogue includes 623 glitches, and the Jodrell Bank catalogue includes 666 glitches. Both of them list, for most events, the name of the pulsar, the moment at which it took place and the relative changes in frequency and first-order spindown, including error bars. The ATNF glitch catalogue also contains the “healing parameter” Q for 118 glitches, which indicates the fraction of frequency change that is recovered after the glitch (Lyne et al. 2010; Haskell & Antonopoulos 2014) and the time τ that it takes for the pulsar to return to a stable state again. Q ranges from 0 to 1, while typical values for τ range from a few days to weeks for most pulsars but can also exceed a year for some of them. These two last variables are relevant for the Yim & Jones (2020) transient mountain model.

We also work with the main ATNF pulsar catalogue (Manchester et al. 2005), which lists the information for more than 3000 pulsars, such as name, position, frequency of rotation and different spindown orders. We access it with the help of the `psrqpy` package (Pitkin 2018). In Appendix A we go through the procedure of matching the three catalogues, eliminating duplicate glitches, and identifying cases with missing parameters. In the end, we are left with 740 unique glitches from 225 pulsars, of which 726 from 217 have all parameters available that we need for our main analysis. These also include two additional glitches collected from the recent literature (Lower et al. 2020; Zubieta et al. 2022).

Typically, relative changes in rotational frequency f_{rot} and first

order spindown \dot{f}_{rot} are, respectively, $\Delta f_{\text{gl}}/f_{\text{rot}} \sim 10^{-11} - 10^{-5}$ and $\Delta \dot{f}_{\text{gl}}/\dot{f}_{\text{rot}} \sim 10^{-5} - 10^{-2}$ (Fuentes et al. 2017). It has been noted before that the distribution of absolute glitch sizes seems to follow a bimodal Gaussian distribution (Fuentes et al. 2017; Ashton et al. 2017; Arumugam & Desai 2022): there is a wider component of minor glitches and a narrower one of major glitches (see also Appendix B). It is customary to identify these two groups of glitches as “Crab-like” and “Vela-like”, respectively. Ashton et al. (2017) obtained a value of $\Delta f_{\text{gl}} = 10^{-5.5}$ Hz as a threshold between the two types of glitches. The actual sizes of known Crab glitches, however, range from approximately 10^{-8} Hz to 1.53×10^{-5} Hz (Shaw et al. 2018), with two glitches above $10^{-5.5}$. On the other hand there are 25 observed glitches from the Vela pulsar, and only 19 of them have $\Delta f_{\text{gl}} > 10^{-5.5}$ Hz. Hence we will not follow the strict distinction into two subpopulations: we will use Crab and Vela as prototypes for pulsars with smaller and larger glitches, respectively, but without implying that all glitches from the same pulsar have the same properties.

3 TCWS FROM PULSAR GLITCHES

3.1 The basic idea

Different models have been proposed to describe the underlying physics of NS glitches (Haskell & Melatos 2015). A leading idea is that they originate from the layered structure of NS interiors (Lyne et al. 2000). For this model it is crucial for there to be a superfluid neutron component in the interior. The measured rotation frequency f_{rot} from electromagnetic observations depends on the evolution of the outer crust and the normal (non-superfluid) component of the NS’s interior coupled to it. For both we can assign the angular frequency $\Omega = 2\pi f_{\text{rot}}$. This frequency decreases over time due to the energy lost as emitted radiation, as measured in pulsar timing. The superfluid component, however, can continue to rotate at a different angular velocity Ω_s . When the difference $\Delta\Omega = \Omega_s - \Omega$ reaches some critical value, an instability takes place and part of the angular velocity of the superfluid component is transferred to the outer crust. As a result, the angular velocity of the outer crust suddenly increases and a glitch occurs. The standard “two-fluid model” (Andersson et al. 2003; Andersson et al. 2004) for this instability, and alternative models, such as “starquakes” (Ruderman 1991; Middleditch et al. 2006), are discussed in more detail in the context of GW emission in Prix et al. (2011). We will not go further into discussing glitch models here. Instead we will only summarize below the specific quantities we need to predict GW emission.

First, we consider the frequency evolution at and after the glitch. When a glitch takes place, we can consider three contributions: the secular spindown of the pulsar before the glitch, the near instantaneous change at the glitch epoch, and often a partial recovery back towards the original frequency. We can express the total change Δf_{gl} in the pulsar’s rotational frequency at the glitch time as the sum of a transient part and a permanent part, and similarly with the change $\Delta \dot{f}_{\text{gl}}$ in the pulsar’s first-order spindown. Changes in higher-order spindown parameters are only measured for very few glitches and not included in the catalogues we use here. Hence, we use the following definition of the change of the frequency of the pulsar due to the glitch:

$$\Delta f_{\text{gl}}(t) = \begin{cases} 0, & \text{if } t < t_g, \\ \Delta f_{\text{gl,p}} + \Delta \dot{f}_{\text{gl,p}} \Delta t + \Delta f_{\text{gl,t}} e^{-\frac{\Delta t}{\tau}}, & \text{if } t \geq t_g, \end{cases} \quad (1)$$

where $\Delta t = t - t_g$ is the difference between the current time t and

the glitch time t_g , τ is the recovery time-scale of the glitch, and $\Delta f_{gl,p/t}$ are the permanent and transient parts of the total change in the frequency of the rotating pulsar. For the first-order spindown, following [Yim & Jones \(2020\)](#), only a permanent change $\Delta f_{gl,p}$ is explicitly included; see Section 6.3 for further details on how this parametrization relates with their model.

Another relevant variable is the healing parameter Q , which quantifies the fraction of transient change in frequency:

$$Q = \frac{\Delta f_{gl,t}}{\Delta f_{gl}}. \quad (2)$$

If $Q = 1$, the pulsar’s frequency f_{rot} from before the glitch is eventually fully recovered, while if $Q = 0$, the pulsar maintains the frequency acquired at the glitch. Inferring Q from pulsar timing requires extended post-glitch observations. Therefore values for Q are only available for a subset of observed glitches. In particular, for some analyses in this paper we have used the 118 glitches with Q listed in the ATNF glitch catalogue ([ATNF 2022](#)) and the Q for one recent Vela glitch from [Zubieta et al. \(2022\)](#).

A standard emission scenario for persistent CWs ([Haskell & Schwenzer 2020](#)) is a mass quadrupole, or “mountain”, which emits at $f_{GW} = 2f_{rot}$. It is reasonable to expect that a “transient mountain” (a deformation that is created at the glitch and dissipates again after a while) would emit tCW-like signals. Such a model was explored in a recent work by [Yim & Jones \(2020\)](#), where the observed change in spindown after a glitch is entirely associated to an extra torque from a transient mountain, which is equivalent to assuming that the spindown change is purely transient. This naturally emits GWs on the timescale of observed pulsar glitch recoveries. We postpone specific constraints for GWs produced by such transient deformations to Section 6, as well as checks of how well the model’s assumptions line up with the glitching pulsar population.

Other models propose different physical mechanisms giving rise to a time-varying quadrupolar moment, such as oscillation modes or circulations inside the NS: e.g. Ekman flows ([van Eysden & Melatos 2008](#); [Bennett et al. 2010](#); [Singh 2017](#)) or Rossby (r -)modes ([Andersson 1998](#); [Friedman & Morsink 1998](#); [Chandrasekhar 1970](#); [Friedman & Schutz 1978](#); [Santiago-Prieto et al. 2012](#)). Our main detectability estimation (Section 5), however, is agnostic of the details of post-glitch models, as it only depends on the overall glitch energy budget.¹

3.2 Indirect energy upper limits

We are interested in an upper bound for the maximum amplitude of a post-glitch tCW signal. Here we partially reproduce the derivation given by [Prix et al. \(2011\)](#), based on the two-fluid model. The energy budget considered here is different from, and larger than, the excess energy liberated in the glitch itself, which in turn yields upper limits for shorter-duration GW emission ([Ho et al. 2020a](#)).

According to the two-fluid model, glitches are sourced by a frequency mismatch (lag) between the normal and superfluid components $2\pi\Delta f_{lag} = \Omega_s - \Omega = \Delta\Omega > 0$. More specifically, as discussed in [Prix et al. \(2011\)](#), the available energy for glitches is bounded by

the excess energy in the superfluid component due to this frequency mismatch:

$$\Delta E_s = \frac{1}{2} \mathcal{I}_s (\Omega_s^2 - \Omega^2) \approx 4\pi^2 \mathcal{I}_s f_{rot} \Delta f_{lag}, \quad (3)$$

where the approximation assumes that $\Delta\Omega$ is negligible with respect to Ω . Under the assumption that each glitch fully restores corotation between the normal and superfluid components, which we take throughout this work, ΔE_s is the relevant energy budget for post-glitch tCW emission. A more detailed discussion of this result is given in Appendix C.

On the other hand, we know that the total energy carried by a quasi-monochromatic GW signal depends on a (time-dependent) amplitude parameter $h_0(t)$, the speed of light c , the gravitational constant G , its frequency f_{GW} , the distance from the source d and the total emission time T :

$$E_{GW} = \frac{2\pi^2 c^3}{5G} f_{GW}^2 d^2 \int^T h_0^2(t) dt. \quad (4)$$

This is proportional to the square of the dimensionless root-mean-square amplitude \hat{h}_0 of a GW signal:

$$\hat{h}_0^2 T = \int^T h_0^2(t) dt. \quad (5)$$

To obtain an upper limit, we can combine equations (3) and (4) imposing $f_{GW} = 2f_{rot}$. This way we describe the maximum value of \hat{h}_0 in terms of the distance d from the pulsar, the moment of inertia \mathcal{I} , the duration T , the glitch size and the rotational frequency:

$$\hat{h}_0 \leq \frac{1}{d} \sqrt{\frac{5G}{2c^3} \frac{\mathcal{I} |\Delta f_{gl}|}{T f_{rot}}}. \quad (6)$$

where $\mathcal{I}_s \Delta f_{lag}$ has been replaced with $\mathcal{I} \Delta f_{gl}$ due to angular momentum conservation and the assumption of corotation getting restored by the glitch (see Appendix C).

If we assume the signal has constant amplitude and lasts for a time $T = \tau_r$, then simply $\hat{h}_0 = h_{0,r}$, and the indirect energy upper limit for such a “rectangular” signal becomes

$$h_{0,r} \leq \frac{1}{d} \sqrt{\frac{5G}{2c^3} \frac{\mathcal{I} |\Delta f_{gl}|}{\tau_r f_{rot}}}. \quad (7)$$

Given that equations (4) and (5) depend on a simple integral of $h_0^2(t)$, if we were to consider an exponentially decaying signal with decay time of $\tau_e = \tau_r$, the only difference in equations (7) and (9) would be an extra multiplicative factor of $\sqrt{2}$. When presenting our results, we discuss the relevant scaling factor where needed, and in most plots we use double axes to show both cases. See Appendix D for an explicit calculation.

Assuming that tCW emission is sourced by a transient quadrupolar moment induced in the star due to an unspecified process caused by the glitch, upper limits on h_0 can be interpreted using the standard expression for the GW amplitude from a non-axisymmetric deformation ([Jaranowski et al. 1998](#)),

$$h_0(t) = \frac{4\pi^2 G \mathcal{I} f_{GW}^2}{c^4 d} \epsilon(t). \quad (8)$$

Here we use the equatorial ellipticity defined from the principal moments of inertia as $\epsilon = |\mathcal{I}_x - \mathcal{I}_y|/\mathcal{I}$, where for consistency with the above equations we use a simple \mathcal{I} for the z component. By equating (8) to equation (7) we obtain

$$\epsilon_r \leq \frac{1}{16\pi^2} \sqrt{\frac{5c^5}{2G} \frac{1}{\mathcal{I} \tau_r} \frac{|\Delta f_{gl}|}{f_{rot}^5}}. \quad (9)$$

¹ r -modes are a special case as their dominant GW emission is at approximately $f_{GW} \approx 4f_{rot}/3$ (with relativistic corrections and dependence on the neutron-star equation of state, see [Yoshida et al. 2005](#); [Idrisy et al. 2015](#)) and hence the detectability estimates for individual glitches will actually be different, though our procedure still applies identically.

This provides a benchmark that indicates the maximum possible ellipticity a pulsar can present due to a transient mountain formed at a glitch, in addition to any long-term ellipticity that it may have. It is independent of the pulsar distance and only depends on the intrinsic properties of the pulsar and the glitch. In this picture, a rectangular signal corresponds to assuming that a transient mountain forms at the glitch, remains at constant size for time τ_r , and disappears instantaneously.

A more specific model for the effects of a transient quadrupolar moment is given by [Yim & Jones \(2020\)](#), according to which the source of tCW emission is a transient mountain built up during or just after the glitch by an unspecified process. We postpone an in-depth discussion of their model to Section 6.1. Regarding energy balance, their argument is that such a transient mountain causes a radiative loss which directly impacts the rotational frequency of the observed pulsar and, thus, can be measured from electromagnetic observations. More specifically, only a fraction Q of the energy transferred to the normal component is implied to be radiated. Consequently, the available budget to be emitted via tCWs under the model is reduced to $E_{\text{tCW}} \approx Q\Delta E_s$. This also reduces upper limits from equations (6), (7) and (9) by a factor \sqrt{Q} .

4 SEARCH METHODS FOR TCWS

In this section we present a brief description of different methods to search for tCWs. Understanding this is crucial for a meaningful detectability estimation, as the sensitivity of a search depends not only on the detector noise curves but also on the search method and the specific setup. We concentrate on searches for signals from known pulsars, though some of the methods could also conceivably be extended to broader searches for unknown sources.

4.1 Transient \mathcal{F} -statistic

A commonly used method in CW detection is the \mathcal{F} -statistic ([Jaranowski et al. 1998](#); [Cutler & Schutz 2005](#)). It is applicable to many kinds of searches (see [Tenorio et al. 2021b](#) for an overview), but here we focus on the variant for tCWs introduced by [Prix et al. \(2011\)](#). This assumes that the signal is equivalent to a truly persistent CW multiplied with a window function that limits its duration and modifies its amplitude evolution:

$$h(t; \theta) = h(t; \lambda, \mathcal{A}, \mathcal{T}) = \omega(t; \mathcal{T})h(t; \lambda, \mathcal{A}). \quad (10)$$

Here θ are all the parameters the signal depends on. $h(t; \lambda, \mathcal{A})$ is a standard CW described by the amplitude parameters $\mathcal{A} = \{h_0, \iota, \psi, \phi_0\}$ (nominal amplitude, inclination angle, polarization angle and initial phase) and phase evolution parameters $\lambda = \{f_{\text{GW}}^{(k)}, \alpha, \delta\}$ ([Jaranowski et al. 1998](#)). These include a certain number of spindown terms $f_{\text{GW}}^{(k)}$ for the intrinsic frequency evolution given by a Taylor expansion, and a GW detector measures an additional time-dependent Doppler shift depending on the sky position (α, δ) .

The transient window function ω depends on a set of transient parameters $\mathcal{T} = \{t_0, \tau\}$, with t_0 the start time and τ a duration parameter. A rectangular window simply turns the signal on at time t_0 , and turns it off after a duration τ_r , and the amplitude $h_0(t) = h_{0,r}$ is constant in between. A more natural expectation for dissipative processes, as discussed in Section 3, is an exponential decay window $\omega(t; \mathcal{T}) = \exp[-(t - t_0)/\tau_e]$ for $t \geq t_0$, for which we denote the initial amplitude as $h_0(t_0) = h_{0,e}$.

Given observed data x , we compare two hypotheses: \mathcal{H}_G states that the observed data consists only of Gaussian stationary noise, while \mathcal{H}_{tS} assumes that it also contains a tCW signal $h(t; \theta)$. The likelihood for the data x in the Gaussian noise case is $P(x|\mathcal{H}_G)$ and the likelihood with a signal is $P(x|\mathcal{H}_{\text{tS}})$. From the ratio $\Lambda(x, \theta) = P(x|\mathcal{H}_{\text{tS}}, \theta)/P(x|\mathcal{H}_G)$, one obtains:

$$\log \Lambda(x; \theta) = \mathcal{A}^\mu x_\mu(\lambda, \mathcal{T}) - \frac{1}{2} \mathcal{A}^\mu \mathcal{M}_{\mu\nu}(\lambda, \mathcal{T}) \mathcal{A}^\nu, \quad (11)$$

where \mathcal{A}^μ is a re-parametrization ([Jaranowski et al. 1998](#)) of the four amplitude parameters, x_μ are the projections of the data x on the basis functions associated with these amplitudes, and $\mathcal{M}_{\mu\nu}$ is the antenna pattern matrix. Summation over up/downstairs indices is implied.

The \mathcal{F} -statistic is the result of introducing the maximum-likelihood estimate into the log-likelihood ratio:

$$2\mathcal{F}(x; \lambda, \mathcal{T}) = x_\mu \mathcal{M}^{\mu\nu}(\lambda, \mathcal{T}) x_\nu. \quad (12)$$

So we are left with a detection statistic only dependent on the λ and \mathcal{T} parameters. The CW case corresponds to evaluating this with a rectangular window over the whole observation time. On the other hand, for tCWs, [Prix et al. \(2011\)](#) introduced two detection statistics: one is $\max \mathcal{F}$, the maximum \mathcal{F} over transient parameters, and the other is a Bayes factor $\mathcal{B}_{\text{tS}/G}$ obtained by marginalizing over them, which is slightly more sensitive in Gaussian noise and more robust in real data ([Tenorio et al. 2022](#)).

In either case this method is fully-coherent over the duration of the signal, meaning that we have to assume a certain phase evolution λ . If this is not exactly known, we have to search a template bank of different λ covering any uncertainties in these parameters. Search sensitivity then also depends on the size of the parameter space covered, as more templates lead to a higher statistical trials factor and an increased threshold is needed to keep a fixed false-alarm probability ([Tenorio et al. 2022](#)).

The transient- \mathcal{F} -statistic method has been used in searches of data from the O2 run ([Keitel et al. 2019](#)) and of O3 data ([Abbott et al. 2022b](#)), with template bank sizes up to $\sim 10^7$. Both analyses used only rectangular search windows, for reasons of efficiency: Evaluating the tCW detection statistics for exponential windows would be computationally significantly more expensive ([Prix et al. 2011](#); [Keitel & Ashton 2018](#)), while using rectangular search windows for exponentially decaying signals gives only a small loss in detection efficiency ([Prix et al. 2011](#); [Keitel et al. 2019](#)).

4.2 Other methods

While the transient- \mathcal{F} -statistic method relies on specific templates for the GW frequency evolution, other methods make much fewer assumptions and can be used to search for more generic signals. The Stochastic Transient Analysis Multidetector Pipeline (STAMP, [Thrane et al. 2011](#); [Thrane & Coughlin 2013](#); [Thrane et al. 2015](#); [Macquet et al. 2021](#)) is an example of such an unmodelled method. It is based on pattern recognition of time-frequency spectrogram data, and can be used in several configurations for signals of varying duration, without imposing a fixed starting time or specific frequency evolution. This makes it computationally cheaper and more robust towards a wider class of GW signals, but less sensitive than the matched-filter \mathcal{F} -statistic for signals that actually do follow the tCW model.

Another approach for identifying GW signals while allowing for flexibility in the time-frequency tracks is based on the Viterbi algorithm ([Viterbi 1967](#)) in combination with a hidden Markov model

(HMM, Suvorova et al. 2016). It finds the most probable sequence of ‘hidden states’ (the intrinsic $f_{\text{GW}}(t)$ of a source) from the observed data. This can be applied on different time-frequency resolved input statistics, for example outputs of STAMP (Banagiri et al. 2019), raw strain power (Sun & Melatos 2019), or the \mathcal{F} -statistic evaluated over short segments of data (Sun et al. 2018). Even in the latter case, it is a *semi-coherent* method as opposed to the fully-coherent transient \mathcal{F} -statistic, because it does not preserve phase information across segments. SOAP (Bayley et al. 2019) is another Viterbi-based method working on Fourier power which has recently been used to conduct all-sky searches for quasi-monochromatic gravitational-wave signals (Abbott et al. 2022a).

Both STAMP and Viterbi have been used before for a variety of searches (e.g., Abbott et al. 2017b, 2019, 2021c,d) including long-duration transient searches for a putative NS remnant of the binary merger GW170817. But while they should be applicable to tCWs from glitching pulsars too, this has not been done in practice yet.

Another semi-coherent search method was developed by Keitel (2016), again based on the \mathcal{F} -statistic. This was devised as a computationally efficient ‘add-on’ for semi-coherent CW searches, evaluating the likelihood for tCWs that happen to match closely enough the fixed duration of segments in that search setup. It has been applied in the Einstein@Home framework (Einstein at Home 2022), but no observational results from it have been reported to date.

The fully-coherent \mathcal{F} -statistic is computationally too expensive to extend beyond the small parameter spaces of known pulsars considering observations of more than a few months. On the other hand, STAMP, Viterbi-based and other semi-coherent methods could in principle also be used to search for signals from unknown sources, or where the glitch has not been noticed in electromagnetic observations due to insufficient observational coverage.

New approaches with even greater computational efficiency and the ability to generalise to flexible signal models can also be expected to become available thanks to novel machine learning techniques. See Cuoco et al. (2020) for a review of such techniques in the GW field. For example, deep learning to search for tCWs from glitching pulsars is studied by Modafferi et al. (2023).

5 OBSERVATIONAL PROSPECTS FROM GENERIC ENERGY UPPER LIMITS

Detecting (t)CWs, or at least putting physically interesting constraints on potential sources, requires improvements in sensitivity over past observing runs. These are expected from the LVK detectors during the O4 and O5 runs (Abbott et al. 2020) and more so with the proposed next-generation detectors like ET and CE.

Current detectors are modified L-shaped Michelson interferometers with arm lengths of 4 km (LIGO) and 3 km (Virgo and KAGRA). ET will consist of 3 detectors in shared tunnels with lengths of 10 km and arm opening angles of 60 degrees (Hild et al. 2011). CE is planned as a single 40 km L-shaped detector with an optional second detector of 20 km or 40 km (Evans et al. 2021). Both concepts also include other improvements in mirrors, lasers, cryogenics, quantum technologies and noise-mitigation measures. They are planned to be functional in the 2030s.

We will first discuss, in this section, the most generic and hence also least constraining upper limits, without specific model assumptions for the post-glitch tCW emission, based solely on the available superfluid excess energy as derived in Section 3.2. Then in Section 6 we will specialise to the transient mountain model by Yim & Jones (2020), for which upper limits are lower, but which allows us to de-

rive additional constraints on the distance reach of searches and the ellipticities that can be probed.

The generic results are summarized in Fig. 1. This compares indirect energy upper limits for the previously observed glitch population to the estimated sensitivity of realistic matched-filter searches with different detector configurations, both as functions of frequency, and for an example duration parameter of $\tau = 10$ days. The energy upper limits on h_0 are computed applying equation (7) to data from the ATNF and Jodrell Bank catalogues, assuming GW emission at $f_{\text{GW}} = 2f_{\text{rot}}$ extrapolated to a reference time corresponding to the O4 run starting time. (Here we analyse 726 glitches with epoch, Δf_{gl} , distance and $f_{\text{rot}}^{(k)}$ available from the catalogues, see Appendix A.) The frequency-dependent sensitivity of searches with different detector configurations is derived from their projected noise curves and a realistic matched-filter search setup in such a way that, for a given glitch, tCWs could be detected (or at least physically constrained) if its marker lies above the corresponding sensitivity curve.

More precisely, these *sensitivity curves* correspond to detectable amplitudes within each frequency band, averaged over some signal population, given a specific search setup, noise curve and amount of data; e.g. $h_0^{95\%}$ at a confidence level of 95%.² To construct these conveniently for different detector configurations, we re-scale the detector noise amplitude spectral densities (ASDs) $\sqrt{S_n}$ by the *sensitivity depth* (Behnke et al. 2015; Dreissigacker et al. 2018) defined as (omitting for simplicity the confidence level on its symbol)

$$\mathcal{D} = \frac{\sqrt{S_n}}{h_0^{95\%}}. \quad (13)$$

Briefly, this states how deep under the noise we expect to be able to detect a population of signals, using a specific search configuration. Hence, larger \mathcal{D} implies a more sensitive search. In search setups with fixed false-alarm probability per frequency band, there is a single depth across all frequencies. As we see below, that is also true to good approximation for the search setups we consider. We can then apply such a single factor for pulsars at different frequencies and for different observing runs of a given detector network. We now discuss how this factor is estimated and scales with various parameters before proceeding to the interpretation of results.

First, just like the indirect upper limits (see equation (7)), sensitivity depth depends on the amplitude evolution window and the duration of tCW signals. In particular, for a tCW search with the transient \mathcal{F} -statistic (as discussed in Section 4.1), the sensitivity depth for rectangular signals of duration τ_r is similar to a fully-coherent CW search of that duration (Keitel et al. 2019), meaning it scales with $\sqrt{\tau_r}$ (Jarunowski et al. 1998; Riles 2022). As derived in Appendix D, the difference between rectangular and exponential amplitude evolution windows with $\tau_r = \tau_e$ is simply an overall factor $\sqrt{2}$ in both upper limits and sensitivity curves ($\sqrt{S_n}/\mathcal{D}_{r/e}$). This scaling is taken into account in the secondary vertical axis in Fig. 1, and scalings with $\tau_{r/e}$ remain the same for both cases. In summary, this implies that the relative detectability of signals with different $\tau_{r/e}$ remains the same.³ Fig. 1 illustrates the case of $\tau_{r/e} = 10$ days, but can be

² This quantity is usually referred to as ‘‘population-based upper limits’’ when CW search results are presented; see e.g. Tenorio et al. (2021b). Also see Wette (2012) for details on population averaging procedures.

³ This is still true when there are gaps in the data, as long as they are small compared to the $\tau_{r/e}$ under consideration and approximately uniformly distributed. There will only be an overall reduction in sensitivity given by the overall duty factor. A counter-example where the scaling of sensitivity slows down notably was the one-month maintenance break in O3.

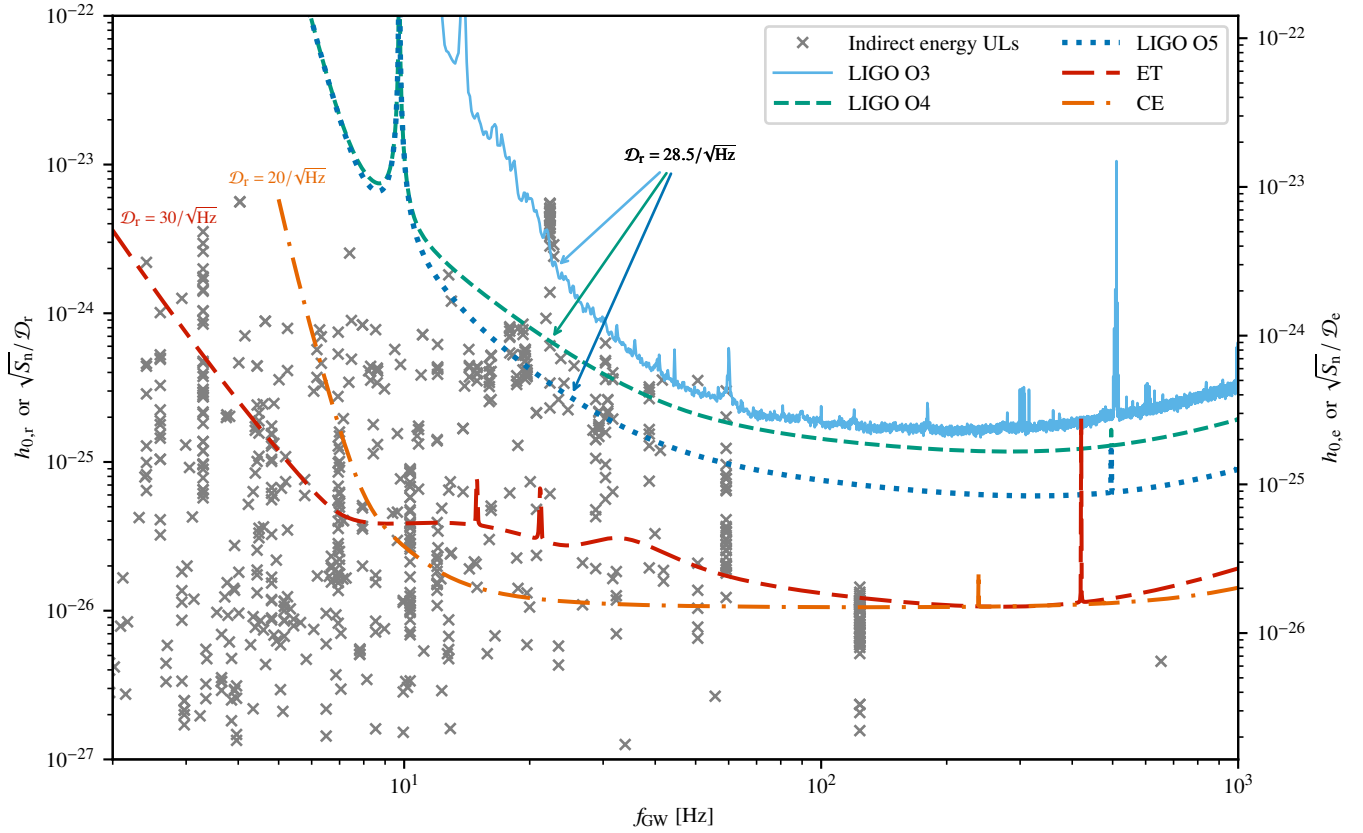


Figure 1. Prospects for detecting or constraining tCWs with current and future detectors, extrapolated from previously observed pulsar glitches. Plotted against GW frequency, the crosses indicate the indirect energy upper limits on GW strain amplitude from a glitch, using the total superfluid excess energy and not assuming any particular emission model. Curves give the expected sensitivity for realistic matched-filter searches with different detector configurations in terms of $\sqrt{S_n}/\mathcal{D}_{r/e}$ (detector noise curve divided by sensitivity depth of a search). For a given glitch, tCWs could be detected or physically constrained with a given detector when the cross is above the corresponding curve. The left-hand vertical axis gives results for “rectangular window” signals (constant amplitude) directly from equation (7). The right-hand axis is for exponentially decaying signals, where both the upper limits and the sensitivity curves scale with the same factor of $\sqrt{2}$. The depth for each detector (network) configuration takes into account the number of detectors and their geometry. This figure illustrates the case of $\tau_{r/e} = 10$ days, but can be easily rescaled to different duration parameters, as both the indirect energy upper limits and sensitivity curves scale with $1/\sqrt{\tau_{r/e}}$. Note that the horizontal axis is $f_{\text{GW}} = 2f_{\text{rot}}$, so that e.g. the stack of crosses near 22 Hz corresponds to Vela and the one near 60 Hz corresponds to the Crab.

easily rescaled to different durations. This assumes that the transient \mathcal{F} -statistic search uses a window function matching the actual signal shape. If a real search uses only the computationally cheaper rectangular window but the real signal decays exponentially, there will be some mild sensitivity loss (Prix et al. 2011; Keitel et al. 2019).

To cover the remaining dependencies (population parameters, statistical properties of the search method, search setup, and the average duty factor, location and geometry of the detectors), we use the numerical sensitivity depth estimation procedure from Dreissigacker et al. (2018), as implemented in OctApps (Wette et al. 2018). One of the inputs needed for this calculation is a threshold on the detection statistic. Our threshold is obtained by first simulating noise-only transient \mathcal{F} -statistic samples matching realistic setups (Keitel et al. 2019; Abbott et al. 2022b; Modafferi et al. 2021) for narrowband searches ($f_{\text{GW}} \approx 2f_{\text{rot}}$) on glitches from Crab and Vela. We then estimate the distribution for the loudest outlier using the method from (Tenorio et al. 2022) as implemented in the `distromax` package (Tenorio et al. 2021a). Details on this procedure are included in Appendix E.

As discussed above, the depth is independent of the detector noise curve, but it still depends on the number of detectors involved and

their geometry. We now discuss the specific detector (network) configurations included in Fig. 1, and the sensitivity depths we obtain.

First, we represent the LVK network by just the two LIGO detectors, which we consider as approximately equally sensitive, as also required by the OctApps implementation. For the last completed observing run O3 we use the harmonic mean of the ASDs from LIGO Hanford and LIGO Livingston taken from Goetz (2021a,b). For the upcoming runs O4 and O5 we use the nominal ASDs from Barsotti et al. (2018). We do not add the less sensitive Virgo and KAGRA detectors (Abbott et al. 2020; Akutsu et al. 2019), so the resulting estimate will be somewhat conservative, though their inclusion in practical searches also depends on computational cost considerations. We find sensitivity depths for Crab and Vela searches of $\mathcal{D}_r \approx 27.5$ and $29.5/\sqrt{\text{Hz}}$, respectively, considering a rectangular signal with $\tau_r = 10$ days. Differences are due to the two pulsars’ distinct sky locations and the different number of templates needed in each search setup, leading to different detection thresholds (see Appendix E). As we will see later in this section, that difference is small enough that we can simplify to using the average $\mathcal{D}_r = 28.5/\sqrt{\text{Hz}}$ for all pulsars, independent of sky position and frequency.

Similarly, for ET and CE we use average depths from the Crab and

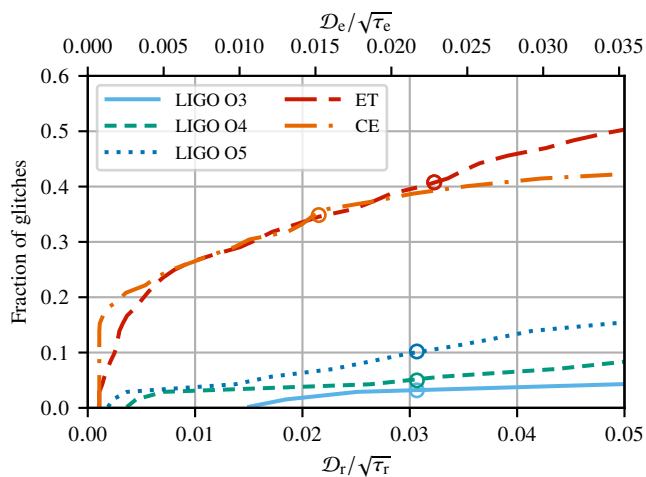


Figure 2. Fraction of previously observed glitches whose tCW emission could be detected or physically constrained with a given detector as a function of search sensitivity depth rescaled by signal duration, using the total superfluid excess energy and not assuming any particular emission model. The circles on each curve represent the depth factors as used in Fig. 1, rescaled by $\tau = 10$ days, for each detector configuration. The lower horizontal axis is for rectangular window signals, while the upper one is for exponential windows. Detectability is the same for both cases, because the scaling of the indirect energy upper limits cancels with that of the depth.

Vela example setups. But the network configurations are different, leading to different depth values. For a single CE detector with the same L-shape geometry as LIGO, assumed to be located in Hanford and with ASD taken from Evans et al. (2020), the depth is similar to a single LIGO detector, $\mathcal{D}_r \approx 20/\sqrt{\text{Hz}}$. For ET, we assume it to be located at the Virgo site. We start from the ASD (ET design team 2018) of a single detector and then estimate the depth including the full triangular observatory geometry; see appendix E. The resulting depth is $\mathcal{D}_r \approx 30/\sqrt{\text{Hz}}$.

The estimated depths just discussed were used for the sensitivity curves in Fig. 1. On the other hand, in Fig. 2 we count how many previously observed glitches would have indirect energy upper limits above the search sensitivity curve, with each detector configuration, when varying the depths. More precisely, we plot against $\mathcal{D}/\sqrt{\tau}$ to remove the dependency on the signal duration. This quantity depends solely on the search method and setup. The figure demonstrates that taking into account a realistic depth for a given search is essential for a fair assessment of detection prospects. On the other hand, small changes in depth do not change the result significantly: the slopes near our estimated values are relatively shallow. This justifies taking the average between Crab and Vela results as approximately representative for all pulsars. The same figure also demonstrates that different detector configurations may reach the physically constraining regime for a very different number of pulsar glitches. This will also be the case for different search methods if their depths differ by more than a few, and at least a qualitatively accurate sensitivity estimation for each approach is crucial in discussing detection prospects. As mentioned in Section 4, we generally expect other, more generic search methods to be less sensitive than the transient \mathcal{F} -statistic, as long as the signals follow the signal model of Prix et al. (2011), but they would still be highly valuable to cover more generic signal types.

In summary, we find that LIGO (or the full LVK network) at design sensitivity should already be able to put physical constraints on tCWs from a small fraction of glitches, reaching below the generic indirect

Table 1. All pulsars for which a transient \mathcal{F} -statistic search in the O4 or O5 runs of the LVK detectors could reach below the indirect energy upper limits from equation (7) for at least one of their previous glitches, using the total superfluid excess energy and not assuming any particular emission model. As discussed in the main text, these results are independent of signal duration. The first three columns list the pulsar name, its approximate GW frequency assuming dominant mass quadrupole emission, and the upper limit for the largest glitch seen from this pulsar, assuming a rectangular amplitude window. The last two columns state how many of the previously observed glitches from each pulsar have such an upper limit above the sensitivity curve from O4 and O5 respectively, and the corresponding percentage.

PSR	f_{GW} [Hz]	max $h_{0,r}$	O4	O5
J0205+6449	30.4	6.3×10^{-25}	3/9 (33 %)	4/9 (44 %)
J0358+5413	12.8	1.8×10^{-24}	0/6 (0 %)	1/6 (17 %)
J0534+2200	59.2	1.2×10^{-25}	2/30 (7 %)	3/30 (10 %)
J0835-4510	22.4	4.7×10^{-24}	21/25 (84 %)	23/25 (92 %)
J0940-5428	22.8	2.9×10^{-24}	2/2 (100 %)	2/2 (100 %)
J1023-5746	17.9	7.9×10^{-25}	0/7 (0 %)	6/7 (86 %)
J1028-5819	21.9	9.2×10^{-25}	1/1 (100 %)	1/1 (100 %)
J1105-6107	31.6	1.9×10^{-25}	2/6 (33 %)	4/6 (67 %)
J1112-6103	30.8	2.6×10^{-25}	0/4 (0 %)	4/4 (100 %)
J1413-6205	18.2	5.3×10^{-25}	0/1 (0 %)	1/1 (100 %)
J1420-6048	29.3	2.2×10^{-25}	0/7 (0 %)	2/7 (29 %)
J1524-5625	25.6	4.4×10^{-25}	0/1 (0 %)	1/1 (100 %)
J1531-5610	23.7	5.0×10^{-25}	0/1 (0 %)	1/1 (100 %)
J1617-5055	28.8	2.6×10^{-25}	0/7 (0 %)	1/7 (14 %)
J1709-4429	19.5	4.8×10^{-25}	0/6 (0 %)	5/6 (83 %)
J1809-1917	24.2	3.4×10^{-25}	0/1 (0 %)	1/1 (100 %)
J1813-1246	41.6	3.6×10^{-25}	1/1 (100 %)	1/1 (100 %)
J1826-1334	19.7	4.6×10^{-25}	0/8 (0 %)	1/8 (12 %)
J1907+0602	18.7	7.9×10^{-25}	0/2 (0 %)	1/2 (50 %)
J1952+3252	50.6	3.5×10^{-25}	1/6 (17 %)	1/6 (17 %)
J2021+3651	19.3	7.8×10^{-25}	0/5 (0 %)	4/5 (80 %)
J2229+6114	38.7	3.1×10^{-25}	3/9 (33 %)	6/9 (67 %)
TOTAL	-	-	36/726 (5 %)	74/726 (10 %)

energy upper limits. But prospects become significantly better with the next generation of detectors, with both CE and ET able to constrain or detect tCWs from a large fraction of the glitch population. To guide searches in the two upcoming LVK runs O4 and O5, we also provide more detailed results in Table 1. This lists all pulsars for which at least one of its previous glitches would have been accessible at O4 and O5 sensitivities, assuming a depth of $\mathcal{D}_r = 28.5/\sqrt{\text{Hz}}$. There are 9 such pulsars for O4 and 22 for O5. Vela (J0835–4510), in particular, is a pulsar of interest for tCW searches not only because it glitches frequently, but also because the majority of its glitches could be detectable in the near future. From the 36 previous glitches from any pulsars accessible at O4 sensitivity, 21 are from Vela (23 out of 74 for O5). The Crab (J0534+2200), on the other hand, has 30 known glitches, but only 2 of them have been large enough for O4 sensitivity (3 for O5). Unfortunately, the “big glitcher” J0537–6910 (Middleditch et al. 2006; Ho et al. 2020b), according to these estimates, is not within reach for O4 nor O5 searches, mostly due to its large distance. Even so, 4 of its known past glitches would have been accessible with the expected ET sensitivity.

6 TRANSIENT MOUNTAIN SCENARIO

The indirect upper limits discussed in Section 5 only assume the overall energy budget of a glitch triggered by two-fluid instabilities and, as discussed by Prix et al. (2011), they also hold approximately for different models, e.g. starquakes. They are therefore independent of specific models for the post-glitch phase: as long as the available

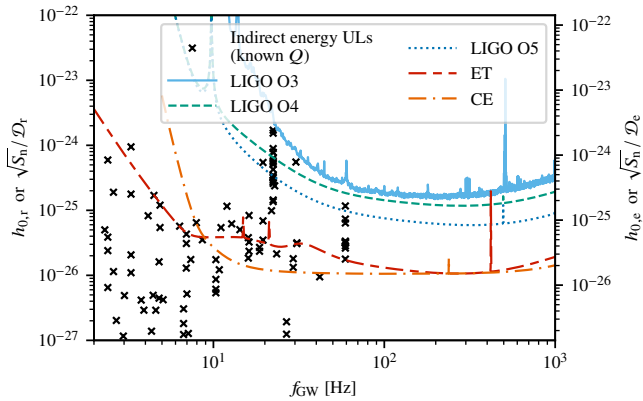


Figure 3. Prospects for detecting or constraining tCWs with current and future detectors, extrapolated from previously observed pulsar glitches, as in Fig. 1; but now assuming the transient mountain model of Yim & Jones (2020) and limited to 119 glitches with known healing parameter Q . The crosses indicate the indirect energy upper limits on GW strain amplitude from a glitch, using equation (14), which are lower than the more generic upper limits in Fig. 1 by a factor \sqrt{Q} . As in Fig. 1, this is calculated for a nominal duration parameter $\tau_{r,e} = 10$ days. Yim & Jones (2020) predict that a tCW signal from a glitch with observed recovery parameter τ should have $\tau_e = 2\tau$. But the detectability of signals is independent of $\tau_{r,e}$, so here we keep the nominal duration fixed to allow for easier visual comparison.

energy is fixed, and completely converted into GWs, the details of this conversion process do not matter for these upper limits. Now we will make a more specific assumption: the tCW signal is emitted by a transient deformation (“mountain”) formed at the time of the glitch.

We will first take the phenomenological model proposed by Yim & Jones (2020) for this scenario at face value and re-estimate observational prospects (Section 6.1) as well as studying the additional constraints on source parameters that could be obtained under the model (Section 6.2). In Section 6.3, we further investigate how consistent the model is with the observed glitch population. We have briefly introduced the model in Section 3. To recap, they consider a transient mountain formed on the pulsar surface at the moment of the glitch, without specifying the formation process. Then, this mountain would dissipate over time during the relaxation phase after the glitch and it would create a braking torque on the NS spinning it back down to near pre-glitch spin frequencies via the emission of tCWs.

6.1 Observational prospects under Yim & Jones model

As briefly discussed before in Section 3.2, the available energy for post-glitch tCW emission can be reduced in this model because, regardless of the specific physical mechanisms of forming a transient mountain, only a fraction of the superfluid excess energy is available for it. This fraction corresponds to the healing parameter Q from equation (2), describing the observation that most pulsars do not completely recover their rotational frequency after a glitch. Hence, the maximum energy radiated after a glitch via tCWs is $E_{\text{tCW}} \approx Q\Delta E_s$, which also still assumes that the glitch restores corotation. Therefore, equation (7) (for rectangular signals) becomes

$$h_{0,r} \leq \frac{1}{d} \sqrt{\frac{5G}{2c^3} \frac{I}{\tau_r} \frac{Q|\Delta f_{\text{gl}}|}{f_{\text{rot}}}} \quad (14)$$

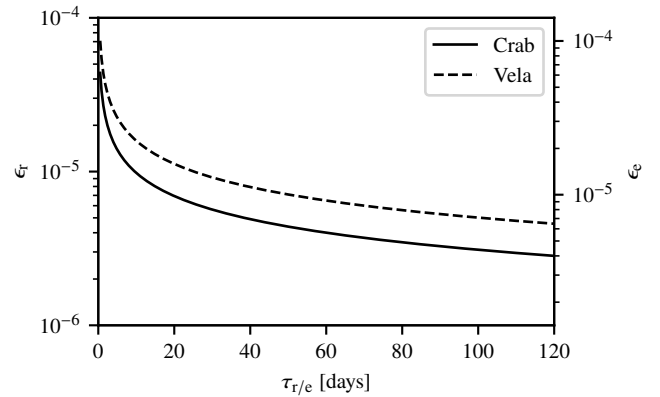


Figure 4. Minimum ellipticity required to detect tCWs from a transient mountain on Crab or Vela with a transient \mathcal{F} -statistic search at ET sensitivity, depending on the duration parameter $\tau_{r,e}$. For the left-hand vertical axis we assume a “rectangular” signal from a constant deformation (ϵ_r), while for the right-hand side the deformation decays exponentially and the plotted ϵ_e is the initial value after a glitch. We have used approximate GW frequencies of 59.9 and 22.4 Hz and distances of 2 kpc and 300 pc for Crab and Vela, respectively, in equation (8).

and the factor $\sqrt{2}$ for exponential signals remains the same. Similarly, for the ellipticity, equation (9) becomes

$$\epsilon_r \leq \frac{1}{16\pi^2} \sqrt{\frac{5c^5}{2G} \frac{Q}{I} \frac{|\Delta f_{\text{gl}}|}{\tau_r} \frac{1}{f_{\text{rot}}^5}} \quad (15)$$

We have used 118 glitches with Q listed in the ATNF glitch catalogue (ATNF 2022), plus the Vela glitch of 2021 with parameters from Zubieta et al. (2022), to recompute upper limits. Results are shown in Fig. 3, again comparing with the estimated sensitivity of transient \mathcal{F} -statistic searches with the same detector configurations as before. The number of glitches for which such searches could reach below these stricter upper limits is significantly reduced compared with Fig. 1 and Table 1: with O4 sensitivity, only 6 previous glitches from Vela and J0205+6449 would have been within reach, and for O5, 14 glitches from 4 different pulsars (the Crab, Vela, J0205+6449 and J1709–4429). ET and CE could still reach below the upper limits for similar fractions as in the generic case: about 37 and 42 % of glitches with known Q , respectively. These two fractions, however, are dominated by Crab and Vela glitches.

We note again, however, that inferring Q from pulsar timing observations is difficult, as demonstrated both by the small fraction of glitches with such a value available and by significant differences in the values listed by ATNF compared with other sources. For example, Crawford & Demiański (2003) (the reference used by Yim & Jones 2020) list Q values for Crab and Vela glitches until 2000. For Vela some of these are larger than those from ATNF, which would correspond to more optimistic tCW upper limits. Also, the postglitch frequency evolution model used by Yim & Jones (2020) includes only one recovery term (matching our equation (1)), while for some glitches ATNF lists up to four pairs of Q and τ parameters, corresponding to multiple exponential recovery components fitted to that glitch. For these cases we choose the maximum Q , which ensures that the upper limit holds in either case, and leave more detailed multi-component modelling to future work.

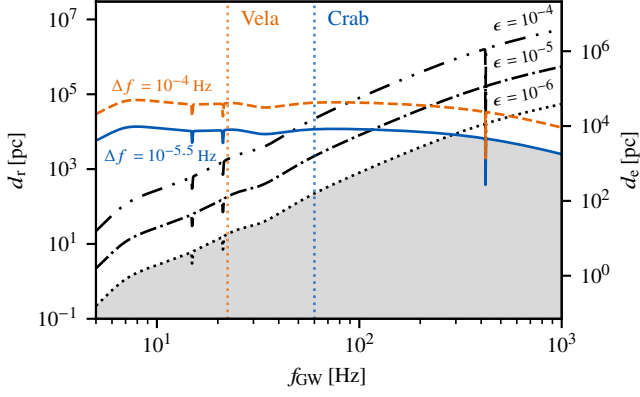


Figure 5. Maximum reach of a transient \mathcal{F} -statistic search with ET for tCWs from glitching pulsars, depending on their GW frequency and for an example duration parameter $\tau_{r/e} = 10$ days. For the left-hand vertical axis we assume a “rectangular” signal, and an exponentially decaying one for the right-hand axis. We compare two different estimates here: The black curves (dotted, dash-dotted and dash-dot-dotted) mark the maximum distance at which we can detect a signal from a transient deformation with a certain (initial) ellipticity, from equation (8). On the other hand, the coloured solid and dashed curves indicate the maximum distance at which we can detect a signal with total energy corresponding to glitch sizes Δf_{gl} of $10^{-5.5}$ and 10^{-4} Hz (corresponding approximately to the largest Crab- and Vela-like glitches, respectively), from equation (14) but assuming $Q = 1$. For orientation, the frequencies of Crab and Vela are also included with dotted vertical lines. Detectable and physically realistic post-glitch signals correspond to the region under both a curve of fixed ϵ and one of fixed Δf_{gl} . For example, the shaded area indicates the ranges for detecting signals with glitch size of $10^{-5.5}$ Hz, $Q = 1$ and with ellipticity of 10^{-6} .

6.2 Achievable reach and ellipticity constraints

Now we consider physical constraints that could be derived from tCW searches under the transient mountain model. We know from equation (8) that for any GW signal coming from a deformed NS with ellipticity $\epsilon(t)$, and emitting at f_{GW} , the strain amplitude $h_0(t)$ is inversely proportional to distance; or for a fixed distance, it tells us the required ellipticity for a certain strain sensitivity. To illustrate this, in Fig. 4 we show the ellipticity constraints for Crab and Vela from the same equation, assuming the sensitivity of ET, fixing the distance and frequency to those of each pulsar, and varying the tCW duration parameter τ . For larger τ we can detect signals from smaller asymmetries.

Since the conversion from sensitivity to constraints on distance and ellipticity depends on the time evolution of the signal amplitude, as before we consider both the rectangular model and the exponentially decaying case. As discussed in Appendix D, results for these two cases only differ by a factor $\sqrt{2}$, and so in this and the following figures we again use two vertical axes for the two cases.

The obtained ellipticities, of the order of 10^{-6} to 10^{-4} for $\tau \leq 120$ days, are still consistent with the latest constraints from LVK searches for persistent CWs from these two pulsars (Abbott et al. 2022c), and a transient mountain could be significantly larger still without violating those CW upper limits. Theoretical constraints on persistent ellipticities (Johnson-McDaniel 2013) depend on the NS equation of state and typically are quoted as 10^{-6} for conventional NS matter and up to 10^{-5} for more exotic equations of state. But for transient deformations it is conceivable that at least the initial value could be higher.

While the detectability statements from Section 5 are independent

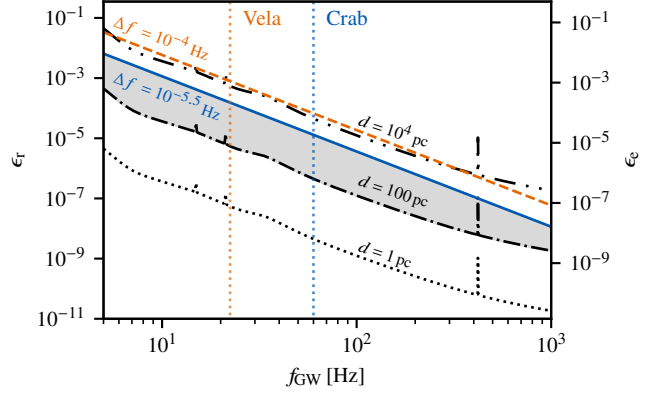


Figure 6. Post-glitch transient ellipticity constraints that could be placed if we detect a tCW of duration $\tau_{r/e} = 10$ days from a glitching pulsar, depending on its GW frequency. For the left-hand vertical axis we assume a “rectangular” signal, and an exponentially decaying one for the right-hand axis. The black dotted, dash-dotted and dash-dot-dotted curves mark the minimum (initial) ellipticity required to detect a signal from a transient deformation on a pulsar at a certain distance, from equation (8) and assuming ET sensitivity. On the other hand, the coloured solid and dashed lines indicate the maximum ellipticity allowed by the energy corresponding to glitch sizes Δf_{gl} of $10^{-5.5}$ and 10^{-4} Hz (corresponding approximately to the largest Crab- and Vela-like glitches, respectively) from equation (15), but assuming $Q = 1$. This does not depend on detector sensitivity, but only on the amount of energy radiated in GWs via a transient mountain. For orientation, the frequencies of Crab and Vela themselves are also included with dotted vertical lines. Detectable and physically realistic post-glitch signals correspond to the region between a curve of fixed distance d and one of fixed Δf_{gl} . For example, the shaded area indicates the allowed ellipticities for detecting signals from a glitch of size $10^{-5.5}$ Hz, $Q = 1$, and a distance of 0.1 kpc.

of τ (because the detection threshold scales the same way as the available glitch energy), Fig. 4 gives the constraints on ϵ we could place in the case of a detection. For this figure we have used a fit for the sensitivity depth as a function of τ (see Appendix E). However, this figure does not take into account whether such ellipticities could actually be produced by a glitch of a certain size. We will combine these considerations in Figs. 5 and 6.

In Fig. 5 we study the reach of tCW searches with ET, i.e. the maximum distance to which signals from glitching pulsars with certain parameters can be detected, as a function of frequency. We compare two different estimates, one for a signal from a transient mountain with a certain (initial) ellipticity, from equation (8), and the other for a signal with total energy corresponding to certain glitch sizes, from equation (7). (The second estimate is generic, not relying on the transient mountain scenario.) Both depend on the amplitude detectable by a search, i.e. the detector noise curve scaled by the τ -dependent sensitivity depth. In addition, from equation (8) we get a scaling with ϵ and f_{GW}^2 , while from equation (7) the scaling is with $\sqrt{\Delta f_{\text{gl}}/f_{\text{GW}}}$. If we then combine both arguments for tCW signals emitted by a transient mountain formed after a glitch, the joint requirement to be both detectable with ET and physically allowed by the glitch energy budget correspond to those signals that come from a distance below both curves for a fixed ϵ and a fixed Δf_{gl} . The figure is for an example $\tau = 10$ days. For different durations, the curves for fixed ϵ will shift upwards with $\sqrt{\tau}$ for larger τ . The curves for fixed Δf_{gl} , however, will stay the same because the τ dependencies cancel when equating the right-hand side of equation (7) with the detectable amplitude: both

emission and detection just depend on the overall energy content, not on its spread over time.

Similarly, in Fig. 6 we show the equivalent curves with the ellipticity ϵ as the dependent variable. Now the one set of estimates comes from equation (8) with fixed distances, and again follows the detector noise curve scaled by sensitivity depth, but with a factor f_{GW}^{-2} . However, the constraint on ϵ from the glitch energy budget, as derived in equation (9), is independent of distance and detector sensitivity, depending only on the intrinsic parameters of the pulsar and glitch and scaling with $f_{\text{GW}}^{-2.5}$. So this is a benchmark that a search needs to pass to give physically meaningful constraints on transient mountain ellipticity. In other words, for a search with ET we only obtain physical constraints in the area between two curves in Fig. 6, namely if the ellipticity is large enough to be detectable from a given distance, but still small enough to not exceed the available energy from a glitch. Again, this is shown for an example $\tau = 10$ days. Both constraints for ϵ from equations (8) and (9) scale with $1/\sqrt{\tau}$, and so both sets of curves would shift downwards for larger τ . But consistently with Fig. 1, the question of whether a certain search can reach the physical benchmark is independent of τ . This is different from the behaviour discussed for Fig. 5 because there the distance constraint from the glitch energy budget was generic (not assuming the transient mountain model), while here, to associate an ϵ to the energy budget, we made this mountain assumption and that makes the τ dependence cancel in equation (9).

In both figures, we have shown example curves for two glitch sizes (dashed orange: $\Delta f_{\text{gl}} = 10^{-5.5}$ Hz, solid blue: $\Delta f_{\text{gl}} = 10^{-4}$ Hz). We chose these as approximately the largest values for Vela- and Crab-like glitches, respectively. For these figures we have implicitly used a factor $Q = 1$. According to ATNF (2022), Crab glitches have typical $Q \approx 0.8$, but typical Vela glitches have much lower values, at most $Q \sim 0.1$. Thus, for realistic Vela glitches the curves in both figures could actually fall below those for Crab glitches.

This pair of plots (Figs. 5 and 6) corresponds to the typical plots of $d(f_{\text{GW}})$ at fixed ϵ and $\epsilon(f_{\text{GW}})$ at fixed d used in CW papers (e.g. Abbott et al. 2021b, 2022a). But as we have seen, for tCWs from glitching pulsars this type of plot depends on additional physical parameters, i.e. the glitch size and signal duration.

6.3 Model checks against observed glitch population

We now discuss the Yim & Jones (2020) model assumptions in more detail and investigate how well the model matches the available pulsar glitch data.

When we introduced equation (1) for the frequency change at a glitch, following Yim & Jones (2020), we included both a transient $\Delta f_{\text{gl,p}}$ and permanent part $\Delta f_{\text{gl,t}}$ but only a permanent part $\Delta \dot{f}_{\text{gl,p}}$ for the spindown change. Taking its derivative with respect to time one obtains the equation for the total spindown change $\Delta \dot{f}_{\text{gl}}$ for times $t \geq t_{\text{g}}$:

$$\Delta \dot{f}_{\text{gl}}(t) = \Delta \dot{f}_{\text{gl,p}} - \frac{\Delta f_{\text{gl,t}}}{\tau} e^{-\frac{\Delta t}{\tau}}. \quad (16)$$

From this we can rewrite the time-dependent coefficient as the transient change in spindown,

$$\Delta \dot{f}_{\text{gl,t}} = -\frac{\Delta f_{\text{gl,t}}}{\tau}. \quad (17)$$

Rearranging this equation and taking also equation (2) one can deduce

$$\Delta \dot{f}_{\text{gl,t}} \tau = -\Delta f_{\text{gl,t}} = -Q \Delta f_{\text{gl}}. \quad (18)$$

This relates the transient spindown change with observationally more accessible quantities: the factor Q , the total frequency change of the pulsar at the glitch, and the recovery timescale τ .

The central assumption of Yim & Jones (2020) is to approximate $\Delta \dot{f}_{\text{gl,t}} \approx \Delta \dot{f}_{\text{gl}}$. That is, to assume that the change in spindown is purely transient, without any permanent part. Under this assumption, they define an approximate timescale

$$\tau_{\text{approx}} = -\frac{Q \Delta f_{\text{gl}}}{\Delta \dot{f}_{\text{gl}}} = \frac{\Delta \dot{f}_{\text{gl,t}}}{\Delta \dot{f}_{\text{gl}}} \tau. \quad (19)$$

This again only depends on parameters that can be directly inferred from pulsar timing. Physically, the approximation corresponds to assuming that no new permanent mountain is formed (or an existing one permanently augmented) at the time of the glitch. In other words, any non-axisymmetry of the pulsar corresponds only to a truly persistent part independent of the glitch (which would emit traditional CWs) and a transient part created by the glitch, that decays again during the recovery timescale.

Comparing τ_{approx} against τ for observed glitches can be used as a consistency check of the model. Even if they do not agree within uncertainties, the case $\tau_{\text{approx}} < \tau$ corresponds to part of the formed mountain being permanent, i.e. events for which one can not fully apply this approximation, but which are still physically reasonable. On the other hand, the case $\tau_{\text{approx}} > \tau$ is physically inconsistent with the transient mountain scenario.

In Yim & Jones (2020), this approximation has been tested for the Crab and Vela pulsars, using benchmarks as discussed below. They obtained generally consistent results, except for the larger Crab glitches and some Vela glitches. Large glitches of the Crab are the only known pulsar glitches that exhibit a measurable permanent change in spindown (Lyne et al. 1993; Lyne et al. 2000). Meanwhile many Vela glitch recoveries require to be modelled by more than one exponential, each with its own τ , and some of its glitches overlap with each other, complicating the estimation of Q .

Here we extend the comparison of their model with observational data to the larger set of 118 glitches with recovery parameters (τ and Q) listed in the ATNF pulsar glitch catalogue, plus the 2021 Vela glitch from Zubieta et al. (2022). (These parameters are not included in the Jodrell Bank glitch catalogue.) To find how well the assumptions of the model match each glitch, we have first compared the tabulated values of τ (including uncertainties) with τ_{approx} calculated from equation (19) (including error propagation). As in Section 6.1, for glitches with multiple recovery components we have chosen the one with the highest Q and the corresponding τ . We find consistent values for 59 glitches out of 119, in the sense that the two uncertainty ranges overlap. Moreover, from the 60 cases with inconsistent τ , 47 have $\tau_{\text{approx}} < \tau$, i.e. are still consistent with a combination of transient and permanent mountain formation. In other words, from 119 glitches, only 13 show $\tau_{\text{approx}} > \tau$, being inconsistent with the transient mountain scenario.

Following this, another consistency check for the model is whether the transient mountains assumed to be formed by a glitch are physically possible, i.e. that the model predicts realistic values of the initial ellipticity right after the glitch. From equation (15), using equation (18) the \sqrt{Q} factor cancels:

$$\epsilon_{\text{approx}} = \sqrt{\frac{-5}{2^9 \pi^4} \frac{c^5}{GI} \frac{\Delta \dot{f}_{\text{gl}}}{f_{\text{rot}}^5}}. \quad (20)$$

With this we can calculate the expected ellipticity of the same 119 glitches. We can then revisit the τ check excluding glitches with unrealistically large ellipticities, which can happen especially for low f_{rot} .

As discussed in Section 6.2, transient mountains could conceivably be larger than the usual constraints on persistent mountains. Also if we impose too strict a cut then the number of selected glitches would be too small to make useful statements. Therefore we choose a rather high example cutoff of $\epsilon < 0.001$. This leaves 73 glitches with available recovery parameters and low ϵ , from which 37 have consistent values of τ_{approx} and τ , and a further 31 have $\tau_{\text{approx}} < \tau$. Hence the fraction of physically reasonable cases only slightly increases after the cut on ϵ : 68 out of 73 glitches.

Finally, we can check another of the assumptions of Yim & Jones (2020), namely that the change in the angular momentum at the glitch is only due to a change in spin frequency, neglecting any change in the pulsar’s moment of inertia. The variables η_1 and η_2 defined in equations (B16) and (B17) of Yim & Jones (2020)⁴ tell us how relevant the changes in the moment of inertia are in the contribution to the angular momentum at the glitch and during recovery after the glitch, respectively:

$$\eta_1 = \frac{-5}{2^{11}\pi^4} \frac{c^5}{GI} \frac{\Delta \dot{f}_{\text{gl}}}{f_{\text{rot}}^4 \Delta f_{\text{gl}}}; \quad (21)$$

$$\eta_2 = \frac{-5}{2^{11}\pi^4} \frac{c^5}{GI} \frac{1}{Q} \frac{\Delta \dot{f}_{\text{gl}}}{f_{\text{rot}}^4 \Delta f_{\text{gl}}}. \quad (22)$$

As suggested by Yim & Jones (2020), values of $\eta_{1,2} < 1$ would imply that neglecting the corresponding changes in the moment of inertia is safe, while larger values indicate that they would contribute significantly to the pulsar’s spin-down. Considering again only the 73 glitches with known recovery parameters and with low ϵ , we find that all have $\eta_1 < 1$ and 58 also have $\eta_2 < 1$. On the other hand, if we do the same test with all 119 glitches with recovery parameters, we find 101 glitches with $\eta_1 < 1$, 64 of which also have $\eta_2 < 1$. In contrast with large values of ϵ , Yim & Jones (2020) suggest that large values of these parameters do not necessarily indicate an unrealistic scenario, but can be compensated by a larger initial event causing the glitch. Hence, one can still consider the transient mountain emission scenario for those glitches, but should be careful with the detailed physical interpretation of putative tCW signals from them.

As a side note, for Crab and Vela, we have obtained some numerical results different from theirs. These are mainly due to different values of Q listed in our source (the ATNF glitch catalogue) compared to their source (Crawford & Demiański 2003).

Summarizing, the model by Yim & Jones (2020) is unlikely to apply to the entire glitch population, but it is consistent with a large fraction of the glitches with reported recovery parameters. A more systematic study could investigate how deviations from the model correlate with various pulsar and glitch parameters, and how these discrepancies should be interpreted physically.

7 CONCLUSIONS

We have estimated detection prospects for quasi-monochromatic long-duration GW transients (tCWs), based on the overall energy budget of pulsar glitches and realistic tCW search setups with the

transient \mathcal{F} -statistic method (Prix et al. 2011; Keitel et al. 2019; Abbott et al. 2022b; Modafferi et al. 2021). We have used a combined set of 726 glitches, mainly from the ATNF and Jodrell Bank catalogues (ATNF 2022; Shaw et al. 2022; Espinoza et al. 2011; Basu et al. 2022).

General prospects are summarised in Fig. 1 under the optimistic assumption of using the whole superfluid excess energy from before a glitch as the budget for post-glitch tCW emission, independent of the tCW emission mechanism. We have found promising prospects for detecting tCWs with the next observing runs of the current LVK detector network or with next-generation detectors, or at least for reaching a physically constraining regime where observational upper limits are below these generic indirect limits. In the O4 and O5 runs of the current LVK detector network, approximately 5% and 10% of known past glitches could be in reach if those pulsars glitch again with similar parameters. Moreover, for the third-generation detectors ET and CE, this fraction increases up to 35–40%.

But we have also explored the more specific assumption of a transient mountain as the emission mechanism, following the model introduced by Yim & Jones (2020). On the one hand, this leads to stricter indirect upper limits, as only a fraction of the energy budget is available for tCW emission from the transient mountain, determined by the glitch healing parameter $0 \leq Q \leq 1$. Together with the smaller number of 119 glitches for which this parameter is available, only 6 and 14 previously observed glitches would be accessible in O4 and O5, respectively, while with ET and CE still about 40% of those with known Q could be within reach. On the other hand, this model allows studying the constraints on physical source parameters that could be obtained by requiring both (i) detectability with a given detector and search setup and (ii) maintaining the glitch energy budget. This yields regions of detectable and physically realistic tCW signals in the space of signal frequency, ellipticity and distance, as illustrated in Figs. 5 and 6.

We emphasize that any such estimation of detection prospects depends on some choice of threshold for declaring a signal as detectable. Here, we estimated the detection threshold using simulated noise distributions for realistic narrowband transient- \mathcal{F} -statistic search setups. This approach takes the “trials factor” of a search properly into account (Tenorio et al. 2022). We recommend using a similar approach whenever possible, rather than referring to a generic signal-to-noise ratio threshold, to ensure that predictions realistically represent actual search capabilities.

We have also extended tests of the transient mountain model’s physical consistency, which Yim & Jones (2020) previously applied to Crab and Vela glitches, to all glitches with recovery parameters included in the ATNF catalogue. We have found that approximately half of the analysed glitches are fully consistent with the model assumption of a purely transient change in spindown (corresponding to a purely transient mountain formed at the glitch). Most others are at least consistent with a mix of transient and permanent contributions, still allowing for some (reduced) tCW emission under this model.

A detailed investigation of the model-specific upper limits for other tCW emission mechanisms, such as Ekman flows or r -modes (see works cited in 3.1 and references therein), is beyond the scope of this work. The generic upper limits would still be expected to cover those cases too, but it would be interesting to compare them more quantitatively against the transient mountain scenario.

On the observational side, searches for tCWs have so far been limited to narrowband analyses of known pulsars (Keitel et al. 2019; Abbott et al. 2022b). Next-generation pulsar surveys, e.g. with FAST (Zhu 2018), CHIME (Amiri et al. 2021) and the SKA (Keane et al. 2015) should enlarge the set of targets for such sources. But

⁴ There is a factor of 1/4 missing on the right hand sides of their two equations, as confirmed by the authors (private communication). As written here, our equations (21) and (22) are consistent with the left hand sides of equations (B16) and (B17) of Yim & Jones (2020), as well as their equation (B13).

other search types over wider parameter spaces could be considered, with the most ambitious goal of blind all-frequency all-sky searches. Besides being less sensitive due to the much higher trials factor, a currently prohibitive issue for such broad searches with the transient \mathcal{F} -statistic method is computational cost (Keitel & Ashton 2018). Alternative semi-coherent or machine-learning methods (e.g. Keitel 2016; Suvorova et al. 2016; Bayley et al. 2019; Cuoco et al. 2020; Modafferi et al. 2023) could make them accessible, but likely still at lower sensitivities than the narrowband coherent matched-filter searches considered here, which hence serve as an overall reference benchmark for the field.

ACKNOWLEDGEMENTS

We thank Garvin Yim and Ian Jones for detailed discussions of their model and on ways to plot sensitivity estimates, Benjamin Shaw for help in tracking down pulsar aliases and rapid corrections of minor typos in the Jodrell Bank glitch catalogue, and the CW working group of the LVK collaborations for discussions and feedback. This work has been supported by European Union FEDER funds; the Spanish Ministry of Science and Innovation and the Spanish Agencia Estatal de Investigación Grants No. PID2019-106416GB-I00/MCIN/AEI/10.13039/501100011033, RED2018-102661-T, RED2018-102573-E; the European Union NextGenerationEU funds (PRTR-C17.I1); the Comunitat Autònoma de les Illes Balears through the Direcció General de Política Universitària i Recerca with funds from the Tourist Stay Tax Law ITS 2017-006 (PRD2018/24, PDR2020/11); the Conselleria de Fons Europeus, Universitat i Cultura del Govern de les Illes Balears; the Generalitat Valenciana (PROMETEO/2019/071); and EU COST Actions CA18108 and CA17137. DK is supported by the Spanish Ministerio de Ciencia, Innovación y Universidades (ref. BEAGAL 18/00148) and cofinanced by the Universitat de les Illes Balears. RT is supported by the Spanish Ministerio de Ciencia, Innovación y Universidades (ref. FPU 18/00694).

The authors gratefully acknowledge computational resources provided by the LIGO Laboratory and supported by National Science Foundation Grants PHY-0757058 and PHY-0823459, and at Artemisa, funded by the European Union ERDF and Comunitat Valenciana, as well as the technical support provided by the Instituto de Física Corpuscular, IFIC (CSIC-UV).

This paper has been assigned document numbers [LIGO-P2200273-v5](#) and [ET-0198D-22](#).

DATA AVAILABILITY

All primary data used in this article were taken from the public ATNF pulsar catalogue (Manchester et al. 2005), ATNF glitch catalogue (ATNF 2022), and Jodrell Bank glitch catalogue (Shaw et al. 2022; Espinoza et al. 2011; Basu et al. 2022); as well as results from Lower et al. (2020) and Zubieta et al. (2022). Results shown in our figures and tables can be easily reproduced from those inputs with the equations in this paper, but tabular data can also be provided upon request.

REFERENCES

ATNF 2022, The ATNF Pulsar Catalogue Glitch Database, accessed 2022 October 11, <https://www.atnf.csiro.au/people/pulsar/psrcat/glitchTbl.html>

- Aasi J., et al., 2015, *Class. Quantum Gravity*, 32, 074001
- Abbott B. P., et al., 2017a, *Class. Quantum Gravity*, 34, 044001
- Abbott B. P., et al., 2017b, *ApJL*, 851, L16
- Abbott B. P., et al., 2019, *ApJ*, 875, 160
- Abbott B., Abbott R., Abbott T., 2020, *Living Rev. Rel.*, p. 3
- Abbott R., et al., 2021a, preprint ([arXiv:2111.03606](#))
- Abbott R., et al., 2021b, *Phys. Rev. D*, 103, 064017
- Abbott R., et al., 2021c, *Phys. Rev. D*, 104, 102001
- Abbott R., et al., 2021d, *ApJ*, 921, 80
- Abbott R., et al., 2022a, preprint ([arXiv:2201.00697](#))
- Abbott R., et al., 2022b, *ApJ*, 932, 133
- Abbott R., et al., 2022c, *ApJ*, 935, 1
- Acernese F., et al., 2015, *Class. Quantum Gravity*, 32, 024001
- Adhikari R. X., et al., 2019, *Class. Quantum Gravity*, 36, 245010
- Akutsu T., et al., 2019, *Nature Astronomy*, 3, 35
- Amiri M., Bandura K. M., Boyle P. J., Brar C., Cliche J. F., Crowter K., Cubranic D., 2021, *ApJS*, 255, 5
- Andersson N., 1998, *ApJ*, 502, 708
- Andersson N., Kokkotas K. D., 1998, *MNRAS*, 299, 1059
- Andersson N., Comer G. L., Prix R., 2003, *Phys. Rev. Lett.*, 90, 091101
- Andersson N., Comer G. L., Prix R., 2004, *MNRAS*, 354, 101
- Arumugam S., Desai S., 2022, preprint ([arXiv:2206.02751](#))
- Ashton G., Prix R., Jones D. I., 2017, *Phys. Rev. D*, 96, 063004
- Bacchetti M., et al., 2020, *ApJ*, 891, 44
- Banagiri S., Sun L., Coughlin M. W., Melatos A., 2019, *Phys. Rev. D*, 100, 024034
- Barsotti L., McCuller L., Evans M., Fritschel P., 2018, Technical Report LIGO-T1800042-v5, Parameters of the A+ design curve (updated version with new coating thermal noise frequency dependence). LIGO Laboratory, <https://dcc.ligo.org/T1800042-v5/public>
- Basu A., et al., 2022, *MNRAS*, 510, 4049
- Bayley J., Messenger C., Woan G., 2019, *Phys. Rev. D*, 100, 023006
- Behnke B., Papa M. A., Prix R., 2015, *Phys. Rev. D*, 91, 064007
- Bennett M. F., van Eysden C. A., Melatos A., 2010, *MNRAS*, 409, 1705
- Chandrasekhar S., 1970, *Phys. Rev. Lett.*, 24, 611
- Crawford F., Demiański M., 2003, *ApJ*, 595, 1052
- Cuoco E., et al., 2020, *Machine Learning: Science and Technology*, 2, 011002
- Cutler C., Schutz B. F., 2005, *Phys. Rev. D*, 72, 063006
- Dib R., Kaspi V. M., Gavriil F. P., 2009, *ApJ*, 702, 614
- Dreissigacker C., Prix R., Wette K., 2018, *Phys. Rev. D*, 98, 084058
- ET design team 2018, Technical Report ET-0000A-18, ET-D sensitivity curve txt file. ET Collaboration, <https://apps.et-gw.eu/tds/?content=3&r=14065>
- Einstein at Home 2022, Einstein @ Home, <https://einsteinathome.org/>
- Espinoza C. M., Lyne A. G., Stappers B. W., Kramer M., 2011, *MNRAS*, 414, 1679
- Evans M., Sturani R., Vitale S., Hall E., 2020, Technical Report LIGO-T1500293-v13, Unofficial sensitivity curves (ASD) for aLIGO, Kagra, Virgo, Voyager, Cosmic Explorer, and Einstein Telescope. LIGO Laboratory, <https://dcc.ligo.org/T1500293-v13/public>
- Evans M., et al., 2021, preprint ([arXiv:2109.09882](#))
- Friedman J. L., Morsink S. M., 1998, *ApJ*, 502, 714
- Friedman J. L., Schutz B. F., 1978, *ApJ*, 222, 281
- Fuentes J. R., Espinoza C. M., Reisenegger A., Shaw B., Stappers B. W., Lyne A. G., 2017, *A&A*, 608, A131
- Glampedakis K., Gualtieri L., 2018, *Astrophys. and Space Science Library*, 457, 673
- Goetz E., 2021a, Technical Report LIGO-G2100674-v1, H1 Calibrated Sensitivity Spectra Jan 04 2020. LIGO Laboratory, <https://dcc.ligo.org/G2100674-v1/public>
- Goetz E., 2021b, Technical Report LIGO-G2100675-v1, L1 Calibrated Sensitivity Spectra Jan 04 2020. LIGO Laboratory, <https://dcc.ligo.org/G2100675-v1/public>
- Haskell B., 2017, *IAU Symp.*, 337, 203
- Haskell B., Antonopoulou D., 2014, *MNRAS*, 438, 16
- Haskell B., Melatos A., 2015, *Int. J. Mod. Phys. D*, 24, 1530008

- Haskell B., Schwenzer K., 2020, *Isolated Neutron Stars*. Springer Singapore, Singapore, pp 1–28, doi:10.1007/978-981-15-4702-7_12-1
- Hild S., et al., 2011, *Class. Quantum Gravity*, 28, 094013
- Ho W. C. G., Jones D. I., Andersson N., Espinoza C. M., 2020a, *Phys. Rev. D*, 101, 103009
- Ho W., et al., 2020b, *MNRAS*, 498
- Idrisy A., Owen B. J., Jones D. I., 2015, *Phys. Rev. D*, 91, 024001
- Jaranowski P., Krolak A., Schutz B. F., 1998, *Phys. Rev. D*, 58, 063001
- Johnson-McDaniel N. K., 2013, *Phys. Rev. D*, 88, 044016
- Keane E. F., et al., 2015, *Proceedings of Science*, AASKA14, 040
- Keitel D., 2016, *Phys. Rev. D*, 93, 084024
- Keitel D., Ashton G., 2018, *Class. Quantum Gravity*, 35, 205003
- Keitel D., et al., 2019, *Phys. Rev. D*, 100, 064058
- LIGO Scientific Collaboration 2021, LIGO Algorithm Library, doi:10.7935/GT1W-FZ16
- Link B., Epstein R. I., Van Riper K. A., 1992, *Nature*, 359, 616
- Link B., Epstein R. I., Lattimer J. M., 2000, *Probing the Neutron Star Interior with Glitches*. Springer Netherlands, Dordrecht, pp 117–126, doi:10.1007/978-94-010-0878-5_14
- Lopez D., Tiwari S., Drago M., Keitel D., Lazzaro C., Prodi G. A., 2022, *Phys. Rev. D*, 106, 103037
- Lorimer D., Kramer M., 2012, *Handbook of Pulsar Astronomy*. Cambridge Observing Handbooks for Research Astronomers, Cambridge University Press
- Lower M. E., et al., 2020, *MNRAS*, 494, 228
- Lower M. E., et al., 2021, *MNRAS*, 508, 3251
- Lyne A. G., Pritchard R. S., Graham Smith F., 1993, *MNRAS*, 265, 1003
- Lyne A. G., Shemar S. L., Smith F. G., 2000, *MNRAS*, 315, 534
- Lyne A., Hobbs G., Kramer M., Stairs I., Stappers B., 2010, *Science*, 329, 408
- Macquet A., Bizouard M.-A., Christensen N., Coughlin M., 2021, *Phys. Rev. D*, 104, 102005
- Maggiore M., et al., 2020, *J. Cosmol. Astropart. Phys.*, 2020, 050–050
- Manchester R. N., Hobbs G. B., Teoh A., Hobbs M., 2005, *AJ*, 129, 1993
- Melatos A., Douglass J. A., Simula T. P., 2015, *ApJ*, 807, 132
- Middleditch J., Marshall F. E., Wang Q. D., Gotthelf E. V., Zhang W., 2006, *ApJ*, 652, 1531
- Modafferi L. M., Moragues J., Keitel D., 2021, *J. Phys. Conf. Ser.*, 2156, 012079
- Modafferi L. M., Tenorio R., Keitel D., 2023, Technical Report LIGO-P2200371, Convolutional neural network search for long-duration transient gravitational waves from glitching pulsars (in preparation). LIGO Laboratory, <https://dcc.ligo.org/P2200371>
- Palfreyman J., Dickey J. M., Hotan A., Ellingsen S., van Straten W., 2018, *Nature*, 556, 219
- Pitkin M., 2011, *MNRAS*, 415, 1849
- Pitkin M., 2018, *J. Open Source Softw.*, 3, 538
- Prix R., Giamparis S., Messenger C., 2011, *Phys. Rev. D*, 84, 023007
- Punturo M., et al., 2010, *Class. Quantum Gravity*, 27, 194002
- Reitze D., et al., 2019, *Bulletin of the AAS*, 51
- Riles K., 2022, preprint (arXiv:2206.06447)
- Ruderman M., 1991, *ApJ*, 382, 587
- Santiago-Prieto I., Heng I. S., Jones D. I., Clark J., 2012, *J. Phys. Conf. Ser.*, 363, 012042
- Shaw B., et al., 2018, *MNRAS*, 478, 3832
- Shaw B., Keith M. J., Lyne A. G., Mickaliger M. B., Stappers B. W., Turner J. D., Weltevredre P., 2021, *MNRAS*, 505, L6
- Shaw B., Lyne A., Mickaliger M., et al., 2022, Jodrell Bank Pulsar Glitch Catalogue, accessed 2022 October 11, <https://www.jb.man.ac.uk/pulsar/glitches.html>
- Singh A., 2017, *Phys. Rev. D*, 95, 024022
- Sun L., Melatos A., 2019, *Phys. Rev. D*, 99, 123003
- Sun L., Melatos A., Suvorova S., Moran W., Evans R. J., 2018, *Phys. Rev. D*, 97, 043013
- Suvorova S., Sun L., Melatos A., Moran W., Evans R. J., 2016, *Phys. Rev. D*, 93, 123009
- Tenorio R., Modafferi L. M., Keitel D., Sintes A. M., 2021a, *distromax*: Empirically estimating the distribution of the loudest candidate from a gravitational-wave search, doi:10.5281/zenodo.5763765
- Tenorio R., Keitel D., Sintes A. M., 2021b, *Universe*, 7, 474
- Tenorio R., Modafferi L. M., Keitel D., Sintes A. M., 2022, *Phys. Rev. D*, 105, 044029
- Thrane E., Coughlin M., 2013, *Phys. Rev. D*, 88, 083010
- Thrane E., et al., 2011, *Phys. Rev. D*, 83, 083004
- Thrane E., Mandic V., Christensen N., 2015, *Phys. Rev. D*, 91, 104021
- Viterbi A., 1967, *IEEE Transactions on Information Theory*, 13, 260
- Wette K., 2012, *Phys. Rev. D*, 85, 042003
- Wette K., Prix R., Keitel D., Pitkin M., Dreissigacker C., Whelan J. T., Leaci P., 2018, *J. Open Source Softw.*, 3, 707
- Yim G., Jones D. I., 2020, *MNRAS*, 498, 3138–3152
- Yim G., Jones D. I., 2023, *MNRAS*, 518, 4322–4329
- Yoshida S., Yoshida S., Eriguchi Y., 2005, *MNRAS*, 356, 217
- Zhu L., 2018, in Heather K. Marshall and Jason Spyromilio ed., *Proc. IAU Vol. 10700, Ground-based and Airborne Telescopes VII*. SPIE, pp 578–591, doi:10.1117/12.2309761
- Zubieta E., et al., 2022, preprint (arXiv:2210.03770)
- van Eysden C. A., Melatos A., 2008, *Class. Quantum Gravity*, 25, 225020

APPENDIX A: PROCESSING OF GLITCH CATALOGUES

The ATNF (ATNF 2022) and Jodrell (Shaw et al. 2022; Espinoza et al. 2011; Basu et al. 2022) glitch tables have substantial overlap, though both tables also contain unique entries. To get the most representative view of the currently known glitch population, we merged the two tables while removing duplicate entries. We also match glitches to pulsars in the main ATNF pulsar catalogue (Manchester et al. 2005) by name to obtain parameters such as distance and frequency.

We find that all the events in the ATNF glitch catalogue have a match in the pulsar catalogue, and for 664 out of the 666 glitches in the Jodrell catalogue we also find correspondence. The remaining entries for which we were not able to match them with pulsar entries in the ATNF catalogue even after some degree of manual checks for spelling variations are the extragalactic X-ray pulsar M82-X2 (Bachetti et al. 2020) and the anomalous X-ray pulsar J1048–5937 (Dib et al. 2009). These cases are excluded from our analysis.

Then, to remove duplicates between the two glitch catalogues, we used the ATNF list as the default, i.e. the parameters listed in it take preference for glitches listed in both tables. We considered two entries from the two catalogues with matching pulsar names as the same glitch if their listed glitch epochs have less than 1 day of difference, or if their uncertainty intervals overlap.

To make sure that we are not missing any repeated glitches, we further manually analysed the 18 pairs of glitches with less than 10 days of difference that have not been removed with the previous step. Comparing the original references for each, we found that 17 of these can be considered as the same. The remaining one from J2301+5852 presents considerably different values of the relative glitch sizes, but even so the dates are very similar – only slightly more than one day of difference. Hence we decided to consider this one as a duplicate as well, falling back to the ATNF parameters as usual.

We are left with the 623 ATNF glitches and 115 additional Jodrell glitches. We also added another glitch of J1105–6910 observed by the UTMOST pulsar timing programme (Lower et al. 2020), which was also analysed in Abbott et al. (2022b), and the recent July 22nd 2021 Vela glitch analysed in Zubieta et al. (2022). This gives us 740 glitches in total from 225 pulsars.

Among these, however, there are some cases with missing parameters that we need for our analyses. For two glitches from J1341–6220 there are no individual glitch size measurements, as discussed in

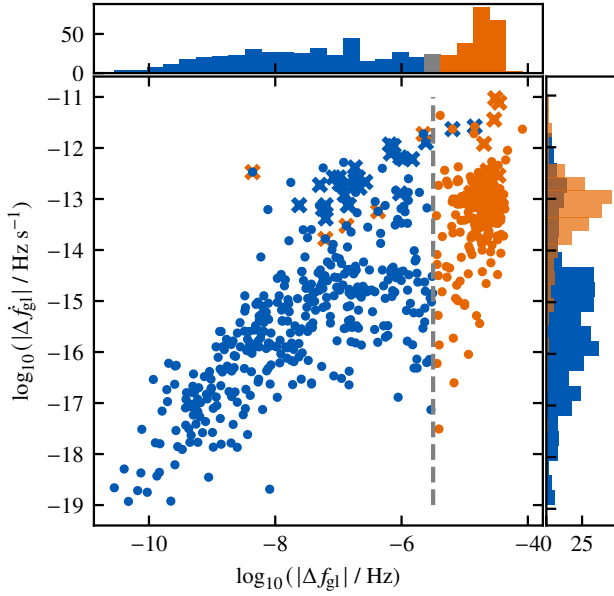


Figure B1. Pairs of $\Delta \dot{f}_{\text{gl}}$ and Δf_{gl} together with histograms of both variables for 627 known pulsar glitches. In blue, Crab-like glitches, and in orange, Vela-like glitches, according to the transition scale $\Delta f_{\text{gl}} = 10^{-5.5}$ Hz from Ashton et al. (2017), indicated by the dashed line.

Lower et al. (2021). Two events from J2301+5852 are “anti-glitches” with $\Delta f_{\text{gl}} < 0$, for which our analysis is not appropriate. Ten more glitches are from 8 pulsars without distances listed in the ATNF pulsar catalogue.

In the end, we use 726 glitches with sufficient information for our main analysis in Section 5, coming from 217 pulsars.

APPENDIX B: SUBPOPULATIONS OF GLITCHES

As discussed in Section 2, the observed glitch population is often categorised into two subpopulations of smaller “Crab-like” and larger “Vela-like” glitches, see e.g. Ashton et al. (2017). To give an updated overview of the latest combined data set of pulsar glitches from the ATNF and Jodrell Bank glitch catalogues (ATNF 2022; Shaw et al. 2022; Espinoza et al. 2011; Basu et al. 2022) as we use them in this work, we provide here two standard plots of relative and absolute glitch sizes in frequency and spindown. Here we use a smaller set (627 glitches from 188 pulsars) than in our main analyses because spindown changes are not catalogued for all events. The transition value of $\Delta f_{\text{gl}} = 10^{-5.5}$ Hz from Ashton et al. (2017) between the two subpopulations (obtained from a Gaussian kernel density estimation fit) is re-used for illustrative purposes, without redoing such a fit.

First, Fig. B1 shows the distribution of absolute glitch sizes, where one can see not only the relatively clear two-Gaussian distribution of frequency steps, but also the correlation between this variable and the spindown change. Vela-like glitches tend to present bigger values of $\Delta \dot{f}_{\text{gl}}$ in a narrower distribution than Crab-like glitches, which also tend to present smaller values of spindown change. On the other hand, there is no clear relation between frequency step size and the original spindown of the source, as was also concluded in Ashton et al. (2017). Similarly, the spindown change is also not clearly correlated with the original spindown of the pulsar.

In Fig. B2 we plot the glitch step sizes variables divided by their original value, i.e. the relative glitch sizes in frequency and spindown,

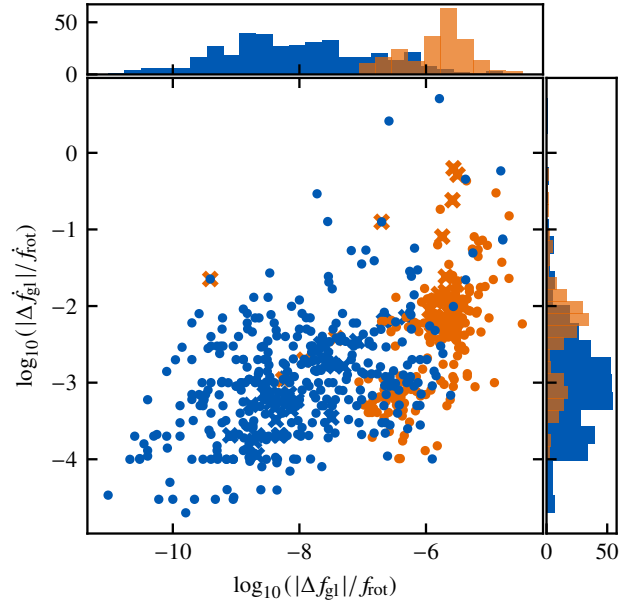


Figure B2. Pairs of $\Delta \dot{f}_{\text{gl}}/f_{\text{rot}}$ and $\Delta f_{\text{gl}}/f_{\text{rot}}$ together with histograms of both variables for 627 known pulsar glitches. In blue, Crab-like glitches, and in orange, Vela-like glitches, according to the transition scale $\Delta f_{\text{gl}} = 10^{-5.5}$ Hz from Ashton et al. (2017).

applying the same categorisation from Ashton et al. (2017) as in Fig. B1. Both the subpopulation distinction and the correlation are less pronounced in these variables.

As already discussed in Section 2, we do not make any explicit distinctions in this paper based on the Δf_{gl} separation criterion. Rather, we just treat Crab and Vela as prototypes for pulsars with smaller and larger glitches, respectively, but taking into account that not all glitches from either pulsar fall on the same side of that division line.

For other studies of pulsar glitch population statistics, see e.g. Espinoza et al. (2011); Fuentes et al. (2017); Lower et al. (2021); Basu et al. (2022); Arumugam & Desai (2022).

APPENDIX C: ENERGY BUDGET FOR POST-GLITCH TCW EMISSION

Here we explain in more detail the use of ΔE_s from equation (3) as the available energy budget for post-glitch tCWs. We use observational constraints on the glitch size, assume that a glitch restores the corotation between the normal and superfluid components of the NS, and assume the typical relation between fiducial moments of inertia as previously done by Prix et al. (2011).

Following the two-fluid model as described in Prix et al. (2011), a glitch corresponds to an energy transfer between the superfluid component and the normal component of a neutron star: the superfluid component slows down by $\delta\Omega_s$ (a negative number) while the normal component spins up by $\delta\Omega = 2\pi\Delta f_{\text{gl}}$.

Typically observed spin-up values of the normal component are such that at most $\delta\Omega/\Omega \sim 10^{-6}$, while no direct observational constraints are available for $\Delta\Omega$ or $\delta\Omega_s$. Under the standard assumption on the fiducial values of the moments of inertia $I_s/I \sim 10^{-2}$, conservation of angular momentum implies $-\delta\Omega_s/\Omega \approx (I/I_s)\delta\Omega/\Omega \sim 10^{-4}$. This implies $\delta\Omega_{(s)}$ can both be

neglected to leading order so that e.g. $\Omega_s + \Omega \approx 2\Omega$. The assumption that corotation is restored after the glitch implies $\Delta\Omega = -\delta\Omega_s + \delta\Omega$, which allows us to relate lag and glitch size as $\Delta\Omega = \delta\Omega(1 - \delta\Omega_s/\delta\Omega) \approx \delta\Omega I/I_s$.

The energy required to decrease the rotational energy of the superfluid component by $\delta\Omega_s$ is

$$\Delta E_{\text{co}} = \frac{1}{2} I_s [\Omega_s^2 - (\Omega_s + \delta\Omega_s)^2] = -\frac{1}{2} I_s (2\Omega_s \delta\Omega_s + \delta\Omega_s^2), \quad (\text{C1})$$

which agrees to leading order with the energy required to spin up the normal component by $\delta\Omega$ if corotation is assumed to be restored. By comparing equations (3) and (C1) we obtain

$$\frac{\Delta E_{\text{co}}}{\Delta E_s} = \frac{-2\Omega_s \delta\Omega_s - \delta\Omega_s^2}{(\Omega_s - \Omega)(\Omega_s + \Omega)} \approx -\frac{\delta\Omega_s}{\Delta\Omega} \approx 1 + \frac{\delta\Omega}{\delta\Omega_s}. \quad (\text{C2})$$

Angular momentum conservation imposes $\delta\Omega/\delta\Omega_s = -I_s/I \sim -10^{-2}$ which implies most of the superfluid excess energy must be transferred directly into the normal component during a glitch. Consequently, we take ΔE_s from equation (3) as the relevant budget to place upper bounds on post-glitch tCW emission. Dropping the assumption of restoring corotation after each glitch would be equivalent to reducing the available budget ΔE_s , with the specific fraction being highly dependent on the specifics of the glitch model and thus left for future work.

Comparing to the derivation in Prix et al. (2011), their E_s corresponds to our ΔE_s , while their E_{glitch} would correspond to $\Delta E_s - \Delta E_{\text{co}}$ and is the relevant budget for short-duration GW emission directly triggered by the glitch (Ho et al. 2020a; Lopez et al. 2022).

APPENDIX D: RECTANGULAR VS. EXPONENTIAL TCWS

Here we clarify some of the relations between tCW signals with either a rectangular window (constant amplitude) or exponential window, following the conventions introduced by Prix et al. (2011).

We start from equation (4) for the total energy in a GW signal, which is proportional to the integral of the squared signal amplitude over the signal duration, and hence also proportional to the square of the root-mean-square amplitude from equation (5):

$$E_{\text{GW}} \propto \hat{h}_0^2 T = \int_0^T h_0^2(t) dt. \quad (\text{D1})$$

Analogously to equation (10) for the full $h(t)$, through $h_0(t)$ this also depends on the tCW window function. For a rectangular window, the integral goes to $T = \tau_r$, which by definition represents the total duration of the signal. In this case, the integral becomes trivial:

$$E_{\text{GW}} \propto \int_0^{\tau_r} h_{0,r}^2 dt = h_{0,r}^2 \tau_r. \quad (\text{D2})$$

For an exponential window, following the convention from Prix et al. (2011) to cut it after $T = 3\tau_e$, the same quantity becomes

$$E_{\text{GW}} \propto \int_0^{3\tau_e} h_{0,e}^2 e^{-\frac{2t}{\tau_e}} dt = h_{0,e}^2 \frac{\tau_e}{2} (1 - e^{-6}) \approx h_{0,e}^2 \frac{\tau_e}{2}. \quad (\text{D3})$$

(The exact choice of the cutoff does not matter as long as $\exp(-2T/\tau_e) \ll 1$.)

Now we will consider signals with either rectangular and exponential shape emitted by the same source, i.e. with the same total energy, and compare the two windows in two special cases which are also illustrated in Fig. D1: either equal duration parameters τ or equal initial amplitudes h_0 . For $\tau_e = \tau_r$, we find that equations (D2) and (D3) enforce $h_{0,e} = \sqrt{2}h_{0,r}$ to have the same total energy in both signals; while for $h_{0,e} = h_{0,r}$ the requirement is $\tau_e = 2\tau_r$. This can

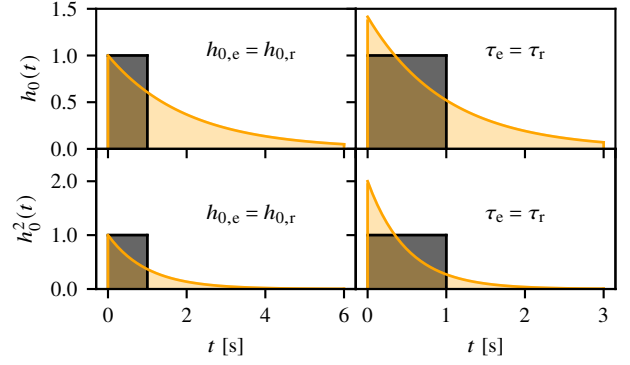


Figure D1. Comparison between exponential and rectangular window functions. In the first column, the two signals with different windows have the same initial strain amplitude $h_{0,r/e}$, and duration parameters $\tau_{r/e}$ are computed from equations (D2) and (D3) to ensure equal total energy. In the second column, $\tau_{r/e}$ are equal for the two windows, and $h_{0,r/e}$ are computed from the same equations for equal total energy. The top row shows the strain amplitude $h_0(t)$, where areas under the curves are *not* equal between the two windows, while in the bottom area $h_0^2(t)$ is shown, with the areas under the curves equal and proportional to the total GW energy.

be visually appreciated in the bottom row of Fig. D1, where areas beneath the curves correspond to the energy, and are equal for the two windows.

We also verified empirically that these relations hold for the implementation of the \mathcal{F} -statistic in LALSuite (LIGO Scientific Collaboration 2021) using the synthesizerTransientStats program (Prix et al. 2011). We simulated signals at different initial h_0 and a fixed duration parameter $\tau_{r/e} = 10$ days with the two windows. We find the value of $h_{0,r/e}$ for which 95% of the signals fall above a certain detection statistic threshold. (We used the same threshold as derived for a realistic simulated search below in Appendix E.) The initial test produced a ratio of $h_{0,e}^{95\%}/h_{0,r}^{95\%} \approx 1.28$, instead of the expected $\sqrt{2} \approx 1.4$. The reason was in the timestamps we were using for the simulated analysis, from the O3 run. Their gaps (especially the month-long maintenance break in October 2019) mean that at equal τ an exponential window (with a total duration cut at $T = 3\tau_e$) does not actually accumulate as much additional signal power compared to the rectangular window with duration $T = \tau$ as in ideal uninterrupted data. With gapless data, the empirical ratio instead is found as ≈ 1.4 .

The main conclusion from the comparison in this Appendix is that our main results, especially the indirect energy upper limits as in Fig. 1, can be converted from rectangular to exponential windows by rescaling any $h_{0,r}$ values with a factor $\sqrt{2}$, as done in the right-hand side vertical axis of that figure. The same scaling applies to the inferred ellipticity constraints in Figs. 4 and 6, and the inverse scaling applies to the sensitivity depth \mathcal{D} from equation (13) and the distance constraints in Fig. 5.

APPENDIX E: SENSITIVITY DEPTH ESTIMATION

To properly determine the expected sensitivity curves of realistic tCW searches with future detectors and compare them with indirect energy upper limits of known pulsar glitches, we have to estimate the sensitivity depth \mathcal{D} defined in equation (13). We do this for two prototypical post-glitch searches, namely those targeting the Crab and Vela pulsars.

Candidates from searches over a template bank, such as the transient- \mathcal{F} -statistic searches we consider here, are usually identified by setting a threshold at a fixed false-alarm probability on the *overall* search, which results in a higher value than that corresponding to a single-template false-alarm probability. Such a threshold, which depends on the extension of the searched parameter space (hence on the number of templates analysed by a search), can be easily estimated from actual or simulated search results after applying `distromax` (Tenorio et al. 2022, 2021a). With this information, and using a realistic duty factor for the detectors, we can use the Dreissigacker et al. (2018) method to estimate the depths \mathcal{D} for different detector configurations.

E1 Number of templates

We consider the Vela glitch of 2016 December 12 (Palfreyman et al. 2018) previously analysed by Keitel et al. (2019) and the Crab glitch of 2019 July 23 (Shaw et al. 2021) analysed by Abbott et al. (2022b). Those were narrowband searches allowing for some flexibility of GW frequency evolution around the pulsar timing solutions, i.e. $f_{\text{GW}} \approx 2f_{\text{rot}}$ and similarly for the spindown parameters. As in those analyses, we assume a search of 120 days of data after the glitch. Following the setup in Modafferi et al. (2021), the widths of frequency and spindown bands suitable for each search are calculated from the pulsar ephemerides. For the Crab the result is the same as in Abbott et al. (2022b), where the procedure from Modafferi et al. (2021) was already used: $N_{\text{temp}} \approx 3.9 \times 10^6$ templates. For Vela, analysed only in the earlier Keitel et al. (2019) study with different template placement, the resulting $N_{\text{temp}} \approx 3.6 \times 10^5$ is lower than the $\sim 10^7$ used previously.

E2 Threshold estimation from mock search results

The general idea is that we need to understand the noise-only distribution of our detection statistic in order to determine how likely are outliers above a certain detection threshold due to noise fluctuations alone, i.e. false alarms. This depends on the number of templates, because more templates mean probing more independent noise realizations. The approach in Tenorio et al. (2022) is to empirically estimate the distribution of the *loudest outlier* of a detection statistic from realizations of the distribution of the detection statistic itself over a certain template bank. This is implemented in the `distromax` package (Tenorio et al. 2021a). Compared to previous approaches, it still works if the distribution of the detection statistic is not known in closed form (as is the case for the $\max \mathcal{F}$ and $\mathcal{B}_{\text{TS/G}}$ statistics for tCWs), and also works robustly on banks with levels of correlation between templates as used in practical searches (non-vanishing mismatch between templates).

To create fake realizations of the distribution of the $\max \mathcal{F}$ -statistic, under the Gaussian noise assumption, we use the `synthesizeTransientStats` program from LALSuite (Prix et al. 2011; LIGO Scientific Collaboration 2021). Per realization, we draw N_{temp} statistic values corresponding to rectangular windowed tCWs over transient search windows of t_0 in $T_{\text{glitch}} \pm 1$ day and $\tau_r \in [0, 120]$ days with time resolutions of 1800 s, and given the position of each pulsar.

We then determine a detection threshold using `distromax`. Following the choice in Abbott et al. (2022b), the detection threshold corresponds to the mean of the estimated distribution of the loudest outlier plus one standard deviation. We have simulated four realizations of the noise distribution for each target, with different random seeds, to control for the variance in estimated thresholds. The $\max \mathcal{F}$ thresholds for Vela vary from 48.8 to 50.1, so we use a rounded value

of 50. In the case of the Crab, thresholds vary from 51.5 to 52.8 and we use a rounded value of 52.

E3 Depth estimation

The final step for the sensitivity depth estimation is based on the procedure from Dreissigacker et al. (2018), implemented in `OctApps` (Wette et al. 2018). This requires the following input parameters: duty factor, mismatch, probability of false dismissal (p_{FD}), detection threshold, sky location and observation time τ_r .

Duty factors represent the fraction of time each detector has been operative during the search. In real observing runs to date, this factor can vary broadly depending on the start time and duration of the analysis. Here we choose a value of 0.66 per detector. We further take the Abbott et al. (2022b) setup as a reference to set values of 0.2 for the allowed mismatch and 0.05 for p_{FD} . The latter also corresponds to the typical UL confidence level.

Finally, we use the thresholds determined in E2, equivalent to setting a probability of false alarm, and the Crab and Vela sky locations. Then, using an observation time $\tau_r = 10$ days, we obtain sensitivity depths of $\mathcal{D}_r \approx 27.5$ and $29.5/\sqrt{\text{Hz}}$ for searches for Crab and Vela glitches respectively, considering the two LIGO detectors.

For ET, the ASD we use (ET design team 2018) in Section 5 is that of a single detector, which corresponds to the combination of one low- and one high-frequency interferometer in the ET-D design (Hild et al. 2011). For the full observatory with its 3 detectors and arm opening angles of 60 degrees, an easy approach is to use a factor of $\sqrt{3} \sin(\pi/3) = 1.5$ compared to a search with unit depth using a single L-shaped interferometer. Instead, we have modified the `OctApps` code to properly account for this geometry through the detector response, with the parameters for a triangular ET at the Virgo site as in LALSuite (LIGO Scientific Collaboration 2021), which means that this factor does not have to be applied separately. This yields sensitivity depths for Crab and Vela glitches of $\mathcal{D}_r \approx 28.2$ and $32.1/\sqrt{\text{Hz}}$, again at $\tau_r = 10$ days.

CE, on the other hand, has the same geometry as LIGO even though its arms are longer. Hence, the sensitivity depths for a single CE detector at Hanford are the same as for LIGO Hanford alone, i.e. for the same signal duration and Crab and Vela respectively, we get $\mathcal{D}_r \approx 18.4$ and $21.6/\sqrt{\text{Hz}}$. The ASD we use in Section 5 corresponds to the “second stage” (CE2) from Reitze et al. (2019). The reference concept in Evans et al. (2021) is one 40 km plus one 20 km detector. With the `OctApps` sensitivity estimation code we cannot directly model such a heterogeneous network, but its depth would be between the mean of these values and that for the two LIGOs. Given the uncertainty in the actual network to be implemented, here we work with the single detector scenario as a conservative assumption.

E4 Depth dependence on signal duration

As discussed in Section 5, sensitivity depths for tCWs (of either window shape) are expected to scale with the square root of the signal duration parameter. For the values just quoted, we have assumed $\tau_r = 10$ days, and most results in the main part of the paper can be easily rescaled to different durations or to exponential windows as discussed in each case. However, we have recomputed the mean of \mathcal{D}_r for searches for Crab and Vela glitches, just like in step E3, with ET at 16 different values of τ_r from 0.5 to 120 days, and fit these values to produce a smooth curve in Fig. 4, obtaining in this case $\mathcal{D}_r \approx \sqrt{91} \tau_r$.

This paper has been typeset from a $\text{\TeX}/\text{\LaTeX}$ file prepared by the author.